ELSEVIER

Surface and Coatings Technology 122 (1999) 136–142

SURFACE & COATINGS TECHNOLOGY

www.elsevier.nl/locate/surfcoat

Discharge diagnosis and controlled deposition of SnO_x:F films by DC-reactive sputtering from a metallic tin target

A. Martel [a,*,1], F. Caballero-Briones [b,c], J. Fandiño [a], R. Castro-Rodríguez [b], P. Bartolo-Pérez [b,c], A. Zapata-Navarro [c], M. Zapata-Torres [c], J.L. Peña [b,c]

[a] *Facultad de Física, Universidad de La Habana, San Lázaro y L, Vedado CP 10400, La Habana, Cuba*
[b] *Applied Physics Department, CINVESTAV-IPN Mérida, AP 73 97310 Merida, Yuc., Mexico*
[c] *CICATA-IPN, Legaria 694, Col. Irrigación, 11500, Mexico City, Mexico*

Received 7 October 1998; received in revised form 8 May 1999; accepted 19 May 1999

Abstract

Fluorine-doped tin oxide (SnO_x:F) films on glass substrates have been prepared by reactive magnetron DC-sputtering in Ar–O_2–Freon plasma from a metallic tin target. We studied the relationship between the discharge characteristics and film properties and found the discharge conditions in which the films belong to the SnO_2 or to the SnO stoichiometry, by proposing a phase diagram for this system. We showed that the film stoichiometry is closely related to the tin valence changes at the target. We found that there is a narrow voltage band and a limit value in the oxygen content where the films have SnO_2 stoichiometry; outside this region SnO films are obtained. We studied the crystallinity and the optical properties of the SnO_2 films. The results show that crystalline films have cassiterite-like diffraction patterns with preferred orientation in the (110) planes. The crystallinity of the films is improved when the discharge voltage and oxygen content increase. A thermal annealing of the amorphous films at 500°C leaves them in the crystalline cassiterite-like form. The films have a transmittance of ~80% in the visible region of the spectrum and a uniform thickness. © 1999 Elsevier Science S.A. All rights reserved.

Keywords: Phase diagram; Reactive sputtering; Thin films; Tin oxide; X-ray diffraction

1. Introduction

Tin oxide films are of great interest owing to their practical applications in technology. Considerable attention has been devoted to the study of physical and chemical properties of tin oxide films [1–8], with applications as conductive electrodes in thin film solar cells, electronic devices and flat panel displays. However, to the best of our knowledge, very few papers related to SnO_2 thin films obtained by reactive sputtering from a metallic target have been published and little is known about the relationship between the processing conditions and film properties in the SnO_2 deposition.

Sputtering is a widely used technique in thin film processing to deposit compound thin films [6–11]. Such films may be sputtered from alloy targets, co-sputtered from different sources, or be reactively sputter deposited. The reactive sputter deposition can be a very complex and nonlinear process, due to the various factors involved. Two operating modes have been described for reactive sputtering discharge [12]: the ‘metallic mode’ and the ‘compound mode’. High sputter rates and, therefore, high reactive gas consumption characterize the former. In the latter the sputter rate and reactive gas consumption are low. The transition between these two discharge modes occurs abruptly at two critical values of the reactive gas flow, depending on the direction of the transition. The main cause of this hysteresis effect has been attributed to the formation of a compound layer in the surface of the target. In order to obtain controlled film properties, such as stoichiometry and thickness, one has to regulate the relative rates of arrival of metal atoms and reactive species to the substrate and to the target. This can be accomplished by controlling the discharge power or cathode voltage, which allows one to regulate the degree of coverage of the target by a compound layer [8–11].

---

* Corresponding author. Tel.: +52-99-8129-60; fax: +52-99-8129-60.
E-mail address: amartel@ff.oc.uh.cu (A. Martel)

[1] Invited researcher at Applied Physics Department, CINVESTAV-IPN Mérida.

PII: S0257-8972(99)00290-X

In this work we used an Sn metallic target, and we study the relationship between the processing conditions and film properties in the reactive deposition of fluorine-doped tin oxide films when the electrical conditions of the target are regulated. We show that film properties can be controlled either by the discharge power or the cathode voltage control when the appropriate conditions are chosen, and propose a phase diagram for the Sn/Ar–O_2–Freon system.

2. Experimental details

The experiments were carried out in a dc-magnetron sputtering system, using a US'Gun II DC Power Supply with an automatic matching network, DC Plasma Products, Inc., USA. The sputtering target was a 7.6 cm diameter, 99.99% purity, tin metallic supplied by Cerac. Inc., USA (effective ring form sputter area: 21.2 cm^2). The substrates employed were Corning 7059 glass, degreased ultrasonically in a dilute detergent solution, rinsed ultrasonically in deionized water and blown dry in N_2 gas before they were introduced into the chamber. The substrate was fixed directly below the target with a target-to-substrate distance of 4 cm. The substrate was not deliberately heated or cooled. Before each experimental run, a pre-sputtering cleaning was performed for 10 min. This time was found sufficient to reach the stationary electrical conditions of the target. High-purity Ar (99.999%), O_2 (99.9%) and tetrafluoroethane (a commercially available Freon) dilute at 1% in argon were used. The gases were introduced through individual needle valves after the vacuum chamber was evacuated to about 10^{-6} Torr by a molecular pump (Pfeiffer TPU 170, USA). The 1% Freon–argon mixture and the oxygen were introduced consecutively at the pressure needed to obtain the desired Freon and oxygen content and then the argon was introduced to reach a total pressure of 10^{-3} Torr. All the pressures were controlled by a precision Bayard–Alpert gage before turn on the discharge; later, the pressures were not monitored because of the noise.

Before preparing the films we did two experiments in order to monitor the discharge behavior. In the first experiment we fixed the current at 390 mA (effective current density of 18.4 mA cm^{-2}) and increased the oxygen content from 0 to 50% while scanning the cathodic voltage. This experiment was carried out first with 0.75% Freon and later without it in order to appreciate the effect that Freon causes. The second experiment was carried out at 0.1% Freon content with the power supply in the constant power mode. We varied the discharge power at different oxygen contents (30, 40, 45 and 50%) while scanning the cathode voltage.

Some films were previously grown varying the Freon content between 0.01 and 0.75%, in order to have a fluorine concentration in the films between 1 and 5 at.%, which was reported as optimal by Borman and Gordon [1] to obtain conductive films. At the lowest Freon value no fluorine was detected, whereas at the highest Freon value a fluorine concentration over 5% was obtained. From this experiment we chose a Freon concentration of 0.1% as the fluorine content was in the desired range. Once the optimal Freon content was found, ten samples were grown at constant voltage mode with different discharge voltages and oxygen contents (30, 40, 45 and 50%). The deposition time was varied between 10 and 30 min. The chemical composition of the films was measured by X-ray photoelectron spectroscopy (XPS), in a Perkin–Elmer PHI 560/ESCA-SAM system with a double cylindrical mirror analyzer and a base pressure of about 10^{-9} Torr. A Siemens D5000 X-ray diffractometer with a Cu Kα ($\lambda = 0.15406$ nm) radiation source was used to identify the crystalline phases present in the films. Transmission spectra between 350 and 900 nm were performed with a Varian Cary 1E spectrophotometer. An illuminated area of 1.3×1.3 cm^2 was used.

3. Results and discussion

3.1. Discharge diagnosis

Fig. 1 shows the results for the first experiment: the cathodic voltage curves obtained as function of the oxygen content for the runs made in the Ar–O_2 and the Ar–O_2–Freon plasmas. Both curves show smooth, almost linear decreases until a voltage value of about 530 V, when a change in their slopes can be noted. This change in slope can be related to the oxidation of the target from Sn^0 to Sn^{2+}, namely, from the 'metal mode' to 'compound mode' in the sputtering process. From this point, in the curve without Freon the voltage

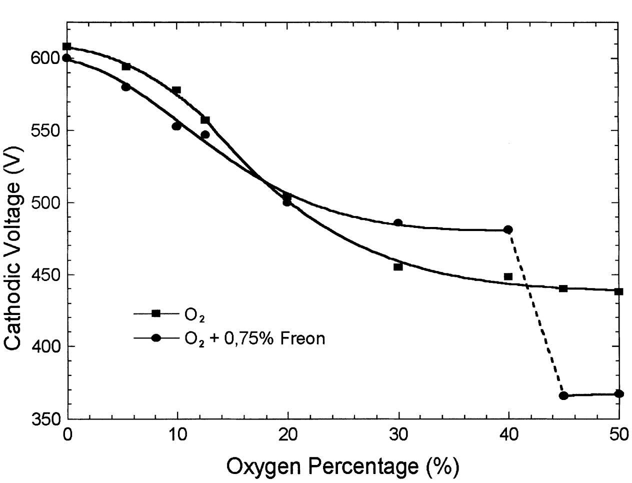

Fig. 1. Cathodic potential at constant current of 390 mA (effective current density of 18.4 mA cm^{-2}) as a function of the oxygen percentage at total pressure of 10^{-3} Torr, with and without 0.75% Freon.

decreases smoothly and reaches a saturation value of about 450 V at an oxygen pressure of 40%. This low voltage value may be caused by oxidation in the target; it can be expected that at high oxygen percentages the target must be fully covered by tin oxide [8–10]. When Freon is introduced into the chamber the voltage shows a similar decay as without Freon, reaching a saturation value of about 485 V with an oxygen content of 30%; however, when the oxygen pressure is increased to 40% the voltage suddenly decreases and reaches a new saturation value (~365 V). This abrupt transition is supposed to be related to the formation of F^-, Cl^-, OF^- or OCl^- radicals in the discharge [11,13]. This highly oxidative atmosphere allows the tin valence to change from Sn^{2+} to Sn^{4+}. The drop in voltage can be attributed to the capability of the tin to react with more oxygen and fluorine when its valence changes [6,7]. The absence of a sudden voltage drop and a single saturation value in the voltage when using only $Ar–O_2$ indicates that the target does not change its valence from +2 to +4, but only gets partially oxidized and so the oxidation takes place mainly at the substrate [7] and the films may present only the SnO stoichiometry. Despite the high oxygen pressure used, it can be said that when using only oxygen as an oxidizing agent the target does not shift from the Sn^{2+} to the Sn^{4+} valence, and the voltage decrease is only related to the discharge chemistry between Ar and O_2 [11]. However, when Freon is present the voltage jumps between two saturation values, where the first saturation value corresponds to Sn^{2+} and the second to Sn^{4+}. For the curve without Freon, the voltage change in the metallic-compound transition is about 120 V. For the curve with Freon the value of the voltage jump (120 V) is equal to the total variation of the cathodic voltage from the metallic tin (605 V) to the first saturation value (485 V). This behavior indicates that tin changes its valence in the target from Sn^0 to Sn^{2+} and then to Sn^{4+}, allowing completely oxidized films (SnO_2 stoichiometry), depending only on the oxygen partial pressure and discharge power used, and that the Sn^0–Sn^{2+} transition requires less energy when Freon is used.

Fig. 2 shows the results of the second experiment: the voltage–power curves of the $Ar–O_2$–Freon discharge. Fig. 2 includes an effective power density axis in order to make the experiment scalable. As we already mentioned above, the Freon presence increases the oxidation state of the tin target, allowing the formation of SnO_2 films. The voltage rises when the power increases, but there are different behaviors depending on the oxygen percentage. Fig. 2 shows four different regions: in the first region (Sn^{4+}-zone) the voltage increases very slowly; in the second region (transition-zone) the voltage rises very sharply; in the third region (Sn^{2+}-zone) the voltage also rises, but it does this more slowly than in the second region, and tends to the fourth region; the fourth region is the Sn^0-zone or metallic target. The regions are wider and better delimited at higher oxygen content; dashed lines in Fig. 2 approximately delimit their boundaries. The discharge stability is poor in the transition-zone, and arcs were often observed in the Sn^{2+}-zone. These results suggest that, when using an $Ar–O_2$–Freon discharge, the more stable oxidation state for the tin is +4. It can be noted that, for the oxygen contents used, the voltage in the Sn^{4+}-zone lies in a narrow band from around 375 V for 50% O_2 to 350 V for 30% O_2. The observed behavior can be explained in terms of the chemical saturation of the target: in the Sn^{4+}-zone a completely oxidized film is formed on the target; at increasing discharge power, when the sputter rate is higher, more oxygen is required to maintain the saturation or the oxide layer tends to be destroyed. We have observed sudden voltage changes through the transition-zone, which correspond with this phenomenon. After the change of the oxide layer, the target tends to become metallic tin, being oxidized at the substrate as Sn^{2+}. These results show that, at sufficiently low discharge power and high oxygen content, it is be possible to obtain controlled stoichiometry, despite the low deposition rate. However, if higher deposition rates are desired, discharge power control may be not suitable, due to the abrupt transitions observed.

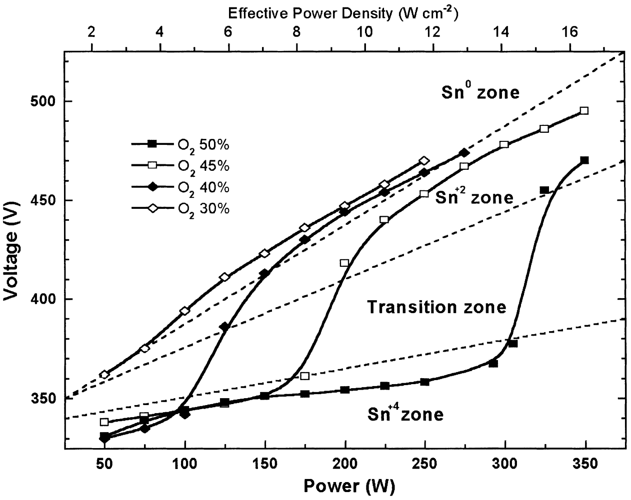

Fig. 2. Discharge voltage–power curves for different percentages of oxygen at total pressure (O_2+Ar+Freon)=10^{-3} Torr, with 0.1% Freon.

3.2. Chemical composition of the films

From the above results we intended to control the cathode voltage to deposit the tin oxide films. Table 1 shows the discharge conditions and the most relevant film characteristics. These experiments were carried out to relate the chemical compositions of the films with the discharge parameters studied. From Table 1 we can see that all the prepared films have a fluorine atomic concen-

Table 1
The discharge conditions and film characteristics

Sample no.	Discharge				Films			
	Target		Pressure[a] (%)		Composition (at.%)			Growth rate (nm/min)
	Power (W)	Voltage (V)	O_2	Ar	Sn	O	F	
P1	70	350	50	49.9	37.2	58	4.8	12.3
P2	150	360	50	49.9	36.4	58.9	4.7	43.3
P3	250	370	50	49.9	33.1	64.4	2.5	111.0
P4	275	375	50	49.9	31.5	66	2.5	128.4
P5	300	390	50	49.9	36.5	61.1	2.4	–[c]
P6	325	450	50	49.9	47.6	51.3	1.1	325.3
P7	200	430	45	54.9	48.8	47.5	3.7	–[c]
P8	260	450	45	54.9	48.0	50.0	2.0	–[c]
P9	215	450	40	59.9	49.8	50.2	–[b]	93.6
P10	360	500	40	59.9	49.2	49.7	1.1	350.0

[a] $P(\mathrm{Ar}+\mathrm{O_2}+\mathrm{Freon})=10^{-3}$ Torr, $P(\mathrm{Freon})=0.1\%$.
[b] Not detected.
[c] Not measured.

tration between 1 and 5%, with deposition rates depending on the voltage. The films P1–P4, prepared at 50% oxygen and voltages less than 375 V, show a mean value of tin atomic concentration of 34.5%, which is very close to the stoichiometric value of the tin dioxide (SnO_2; 33.3% Sn). We consider these films as stoichiometric films of SnO_2. However, for higher voltages or lower oxygen pressures (films P6–P10) the stoichiometry of the films tends to be tin monoxide (SnO; 50% Sn).

Fig. 3 shows the localization of the film growth processes voltage–power curves already explained. The difference between film points and the respective curves is due to different operation modes and processing times.[2] This figure can be considered as the system phase diagram. In the above phase diagram, the SnO and SnO_2 phases are separated by a forbidden zone (the transition one); as can be seen from Figs. 2 and 3, neither curve-points nor film-points were found in this region.[3] The points belonging to the SnO_2 stoichiometry films (P1–P4) fall in the Sn^{4+}-zone, explained before as a region where the target is covered with an SnO_2 layer. The film P5, which still has SnO_2 stoichiometry, is placed at the beginning of the transition zone. The film P6 (50% oxygen), is placed on the Sn^{2+}-zone of the corresponding curve and it has SnO stoichiometry. For the P1–P6 films it is evident that there is not a linear relationship between voltage applied and power measured as was expected from the results of other authors [8,9]. The films obtained with less oxygen pressure than 50% (P7–P10) also have SnO stoichiometry, and they are in the Sn^{2+}-zone of the respective curves. These results show that the regions delimited in Fig. 2 really correspond to the phase diagram (Fig. 3) of the Sn/Ar–O_2–Freon system, and that there is only a narrow band in which the films have the stoichiometry of SnO_2. This band is pointed out in Fig. 3. The band width is about 25 V and the mean value of voltage

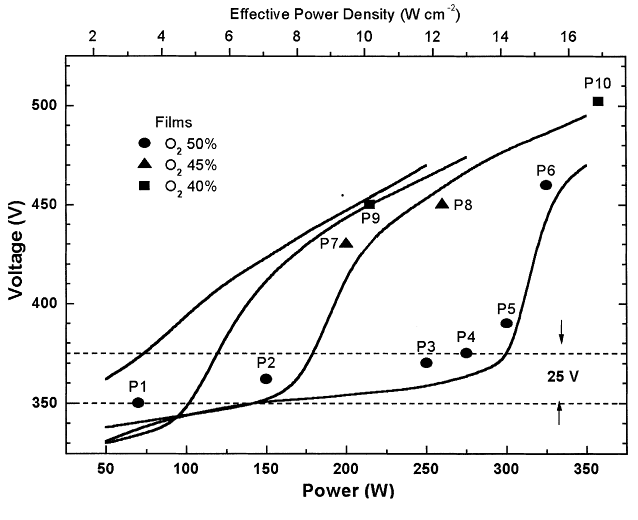

Fig. 3. Film growth processes (P1–P10) in the constant voltage mode located on the discharge power–voltage curves, phase diagram, for different percentages of oxygen under the same pressure conditions as in Fig. 2. (Axes are exchanged to relate with Fig. 2).

---

[2] Each film-point represents an independent experiment, which was done over a long time (10 min of pre-sputtering plus 10–30 min for the film), in the fixed voltage mode. For this long time the discharge becomes very well established. The curve was done in one experiment in the fixed power mode. In this mode, the voltage rises after the power is fixed: at first rapidly, then slowly. The pre-sputtering time for each curve point was 5 min. At this time the voltage is established, but at a long time the curve shifts towards higher voltage values.

[3] The current–voltage (*I–V*) curves can be plotted from the power–voltage data. This plot shows a negative slope for the higher oxygen content in the transition-zone. This demonstrates that the above zone is properly a transition and forbidden one.

(367.5 V) is practically the same as the second saturation value of the cathodic voltage in the Ar–O_2–Freon mixture (~365 V) shown in Fig. 1. It has been pointed out that the constant voltage mode allows one to fix the degree of oxidation of the target surface [8–10] and to avoid the instabilities inherent in the constant current (or power) mode. However, some reactive gas–metal systems cannot be controlled with this method [10]. Our results show that the Ar–O_2–Freon mixture and the metallic Sn target belong to this case. The observed behavior is supposed to be due to the occurrence of a valence change in Sn from 0 to +2 and later to +4 in the presence of the Ar–O_2–Freon plasma, as we have already explained. This change of valence causes an inherent instability in the target oxidation rate, because the Sn^{2+}/Sn^{4+} ratio in the target would be very difficult to control and an additional problem is that the oxidation in the substrate can change in a nonlinear way the Sn^{2+}/Sn^{4+} ratio in the film [6,7]. Thus, absolute control of the stoichiometry in the whole range of oxygen pressures and voltages is very difficult without a feedback control of gas pressures during the entire process and it may be necessary to bias the substrate to control the degree of oxidation of the arriving tin in there.

3.3. Structural characterization of SnO_2 films

Since SnO_2 films are more widely used in microelectronics and other applications than SnO, we focused our attention on the SnO_2 film properties and their relationship with the growth conditions. In Fig. 4 are shown the X-ray diffraction patterns for the SnO_2 films. It can be seen that the film P1 has an amorphous nature, whereas P4 (grown at a higher voltage) has the best crystallinity of all and showing the (110), (101), (200), (211) and (311) cassiterite-related diffraction peaks. This means that the films became more crystalline as the voltage was increased. This improvement of the crystallinity can be associated with the heating of the substrate by increased ion bombardment, particularly by oxygen ions, which also causes more oxidation and, consequently, a closer SnO_2 stoichiometry, as shown in Table 1. These effects may improve the coalescence of the clusters during the film growth. In contrast, for the P1 film there is less heating and less oxygen impingement present and, consequently, an inferior crystallinity and SnO_2 stoichiometry were obtained. To investigate the role of substrate heating in the structural properties of these films, we prepared the P11 film in duplicate. It was deposited using the same conditions as the P1 film, but the substrate was heated at 500°C during growth. A thermal annealing of the films P1 and P11 was carried out in air at 500°C for 6 h. The X-ray diffraction patterns of the P1 and P11 films before and after thermal annealing are shown in the Fig. 5. The as-grown P11 film shows an X-ray pattern very similar to that of the P4 film, without noticeable changes after the annealing, except a slight narrowing of the (110) and (211) peaks. The P1 films shows more remarkable changes after thermal annealing, becoming crystalline with three strong cassiterite peaks: (110), (101) and (211). These results show that the heating of the substrate and the

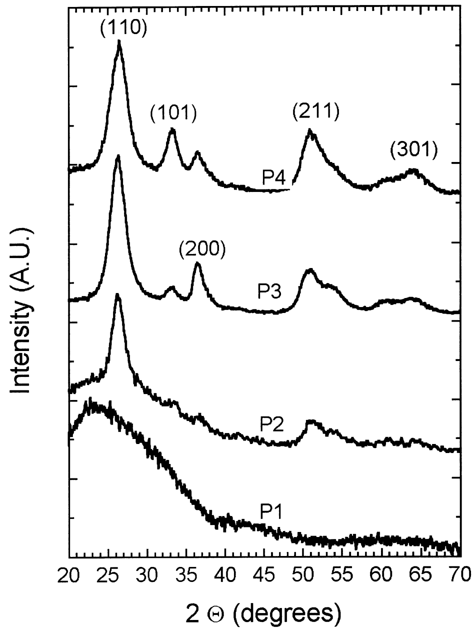

Fig. 4. X-ray diffraction patterns of the SnO_2 stoichiometric films grown without intentional heating at different discharge voltages (P1: 350 V; P2: 360 V; P3: 370 V; P4: 375 V).

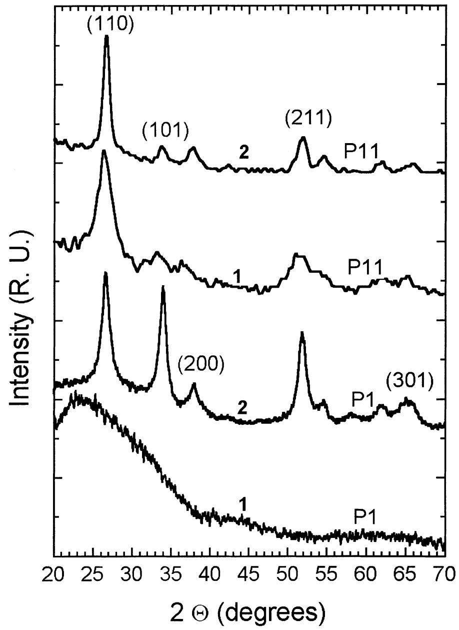

Fig. 5. X-ray diffraction patterns of two SnO_2 stoichiometric films (P11 intentionally heated at 500°C during the growth, and P1 not heated): (1) before thermal annealing; (2) after 6 h of thermal annealing in air at 500°C.

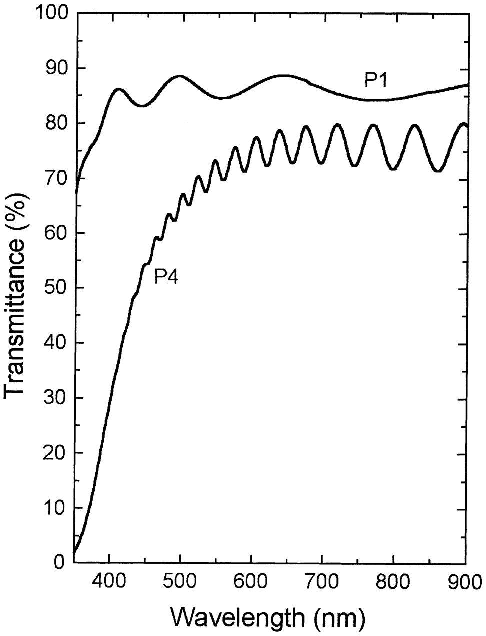

Fig. 6. Transmittance spectrum of transparent, P1 (370 nm) and P4 (2568 nm) SnO_2:F films.

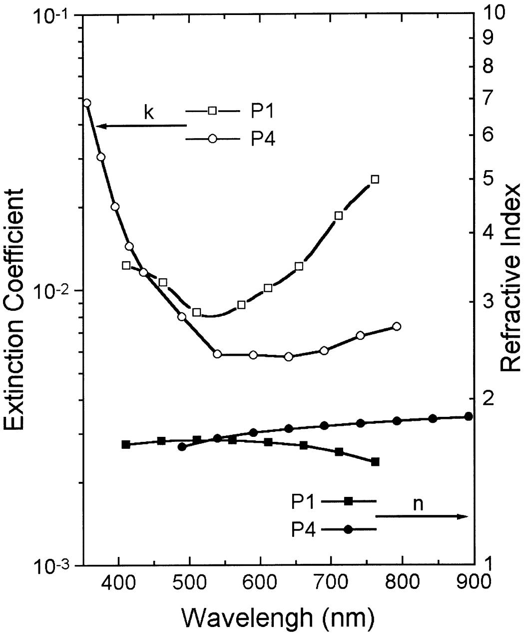

Fig. 7. Dispersion curves of the refractive index *n* and the extinction coefficient *k* for the P1 and P4 SnO_2:F films.

improved oxidation caused by ion bombardment are responsible for the better structural and stoichiometric properties of the P4 film.

3.4. Optical properties of the SnO_2 films

Fig. 6 shows the spectral transmittance measurements for the P1 film (370 nm thickness) and the P4 film (2568 nm thickness). The substrate effect was not included in the measurements. The curves show that for both films the transmittance is about 80% in the 500–900 nm wavelength region and they have good thickness uniformity. These values of the transmittance agree well with the results reported by Di Giulio et al. [4] for good transparent films. The optical constants *n* and *k* of the films were calculated using the method developed by Manifacier et al. [14], and the results are shown in Fig. 7. The dispersion curves of the refractive index agree well with the results of Di Giulio et al. [4] for SnO_2 films obtained by spray pyrolysis. However, the curves of the extinction coefficient do not agree with the results of these authors. This difference must be interpreted in terms of the absorption mechanisms in the visible region of the spectrum ($h\nu < E_g$), which is dominated by band tails and defects that are particular for each method.

4. Conclusions

Experimental conditions for the controlled growth of fluorine-doped tin oxide films on Corning 7059 glass substrates by reactive DC-sputtering in an Ar–O_2–Freon plasma from a metallic tin target were investigated. A phase diagram was proposed and described for the Sn/Ar–O_2–Freon system. We found that the behavior observed is related to the valence changes in the tin target from Sn^0 to Sn^{2+} and then to Sn^{4+} when Freon is added. It was shown that the chemical composition of the films is closely related to the voltage and oxygen pressure in the voltage control mode and that there is a narrow band of voltage and oxygen partial pressure where the films have the SnO_2 stoichiometry; outside of this region the SnO stoichiometry was obtained. We found that both discharge power and voltage control modes in the film growth have individual disadvantages. This is because of the complex chemistry in the plasma and the valence changes in the target, in conjunction with tin oxidation in the substrate. Biasing the substrate and gas control feedback system has been proposed to control the film stoichiometry better. We found that the crystallinity of the SnO_2 stoichiometric films becomes better when the discharge voltage increases. This is due to the improved oxidation and the heating of the substrate by ion bombardment at high voltages and oxygen contents. Well-defined (110), (101) and (211) cassiterite peaks were obtained at these conditions. We have calculated the optical constants *n* and *k* of the films and found good agreement (for *n*) with those reported by other authors.

Acknowledgements

The authors would like to thank their colleagues of the CINVESTAV-Merida: Dr. Oscar Ares for the useful discussions, Dr. Patricia Quintana for the XRD measurements and W. Cauich, F. Gamboa M. Herrera, O. Gómez, O. Ceh and R. Sánchez for the technical support. We also thank L. Pinelo and C. Simon for secretarial assistance. This work was partially supported by CONACYT (Mexico) under project number 211085-5-23676P-E9509.

References

[1] C.G. Borman, R.G. Gordon, J. Electrochem. Soc. 136 (1989) 3820.

[2] R.G. Gordon, in: D. Ginley, A. Catalano, H.W. Schock, C. Eberspacher, T.M Peterson, T. Wada (Eds.), Thin Films for Photovoltaic and Related Device Applications, Proceedings of the Materials Research Society Symposium vol. 426, Materials Research Society, Pittsburgh, PA, 1996, p. 419.

[3] C.F. Wan, R.D. McGrath, W.F. Keenan, S.N. Frank, J. Electrochem. Soc. 136 (1989) 1459.

[4] M. Di Giulio, D. Manno, G. Micocci, R. Rella, P. Siciliano, A. Tepore, Solar Energy Mater. Solar Cells 31 (1993) 235.

[5] B. Robertson, E.P. Lukashev, Biophys. J. 68 (1995) 1507.

[6] A. Zapata-Navarro, M. Zapata-Torres, V. Sosa, P. Bartolo-Pérez, J.L. Peña, J. Vac. Sci. Technol. A: 12 (1994) 714.

[7] F. Caballero-Briones, A. Zapata-Navarro, P. Bartolo-Pérez, R. Castro-Rodríguez, M. Zapata-Torres, W. Cauich, J.L. Peña, Rev. Mex. Fis. S3 (1998) 268.

[8] A.E. Delahoy, M. Cherny, in: D. Ginley, A. Catalano, H.W. Schock, C. Eberspacher, T.M Peterson, T. Wada (Eds.), Thin Films for Photovoltaic and Related Device Applications, Proceedings of the Materials Research Society Symposium vol. 426, Materials Research Society, Pittsburgh, PA, 1996, p. 467.

[9] K. Koski, J. Hölsa, P. Juliet, Thin Solid Films 326 (1998) 189.

[10] J. Affinito, R.R. Parsons, J. Vac. Sci. Technol. A: 2 (1984) 1275.

[11] L. Pekker, Thin Solid Films 312 (1998) 34.

[12] S. Berg, H-O. Blom, M. Moradi, C. Nender, T. Larsson, J. Vac. Sci. Technol. A: 7 (1989) 1225.

[13] E. Stoffels, W.W. Stoffels, D. Vender, G.M.W. Kroesen, F.J. de Hoog, J. Vac. Sci. Technol. A: 13 (2051) 1995.

[14] J.C. Manifacier, M. De Murcia, J.P. Fillar, Thin Solid Films 41 (1977) 127.

PERGAMON

Solid-State Electronics 43 (1999) 2075–2079

SOLID-STATE ELECTRONICS

Effects of high temperature annealing of aluminum at the back of n^+-p-p^+ silicon solar cells upon their spectral and electrical characteristics

Arturo Morales-Acevedo[a,*], Guillermo Santana[a, b], Andrés Martel[a, b], Luis Hernández[a, b]

[a]Centro de Investigación y de Estudios Avanzados del IPN, Electrical Engineering Department, Avenida IPN No. 2508, Mexico DF 07360, Mexico
[b]IMRE-Facultad de Física de la Universidad de la Habana, Cuba

Received 17 April 1999; accepted 7 June 1999

Abstract

Aluminum is usually deposited and alloyed at the back of n^+-p-p^+ silicon solar cells for making a good ohmic contact and establishing a back electric field which avoids carrier recombination at the back surface. Typically, the aluminum thermal treatment is made at temperatures around 600°C for short periods (10–30 min). However, recently it has been suggested that the alloyed region could act as a metallic impurity 'getterer', but still little work has been done on this phenomenon. Therefore, we have made experiments in order to observe the effect that different annealing treatments of the aluminum have on the characteristics of solar cells. In this paper, we show that short-circuit current and open-circuit voltage both improve when aluminum is annealed at temperatures of 800°C for 40 min, when compared to the typical aluminum thermal annealing (600°C for 10 min). From spectral response measurements, we determined that there was improvement of the base minority carrier effective diffusion length due to the high temperature aluminum annealing. Furthermore, from DLTS measurements we have determined that the iron concentration in the base is reduced when the annealing is made at 800°C for 40 min. In other words, there appears to be real metallic 'gettering' by the high temperature treatments, since the improvement seems to be due to the reduction of the recombination centers in the base when iron is extracted from it. These results are encouraging and further experiments will be made in order to improve even more the conversion efficiency of silicon solar cells. © 1999 Elsevier Science Ltd. All rights reserved.

---

1. Introduction

Silicon solar cells made from p-type base material, in addition to the n+ diffused emitter, require the formation of a p+ region at the back with two main purposes:

1. to have low contact resistance at the back;
2. to create an electric field (minority carrier reflector) which reduces carrier recombination at the back surface.

The p+ region is made by deposition of aluminum and alloying it at the back of the cell. In order to do this, a solid phase solution of aluminum in silicon is

---

* Corresponding author. Tel.: +52-5-747-7000; fax: +52-5-754-7697.

E-mail address: amorales@gasparin.solar.cinvestav.mx (A. Morales-Acevedo)

PII: S0038-1101(99)00175-6

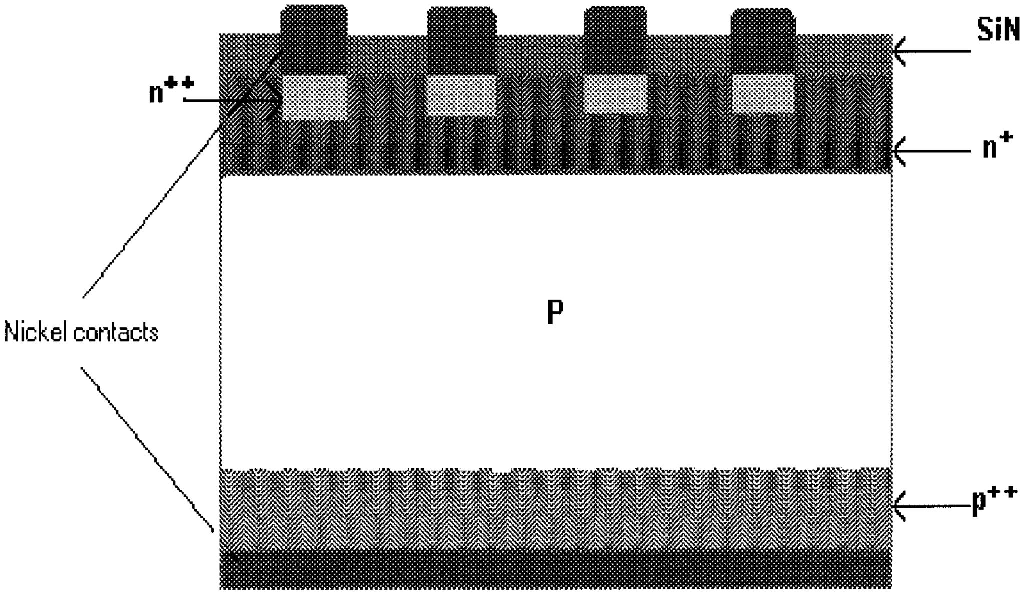

Fig. 1. Schematic of the Selective Emitter Solar Cells fabricated in this work.

formed by annealing the deposited aluminum above the eutectic temperature (575°C). Typically, the aluminum is annealed at 600°C for times between 10 and 30 min [1,2]. However, it has been suggested that the great amount of dislocation and stresses induced at this surface, because of this process, could cause a metallic 'extrinsic gettering' effect [3–5]. This phenomenon would be beneficial for the efficiency of solar cells since metallic impurities usually produce deep levels in the silicon bulk, degrading the minority carrier diffusion length. In order for this 'gettering' phenomenon to occur, the metallic impurities introduced in the material during the fabrication of the cells must diffuse from the bulk to the surface region. Here there is a high segregation coefficient for these impurities due to the high concentration of defects [1]. In order to help the metallic diffusion, the temperature must be increased to values above the typical aluminum alloying temperature, for example between 700 and 800°C.

Hence, a systematic study about the effect that an annealing process, of the aluminum at the back of silicon solar cells, has on the open-circuit voltage and short circuit current should be made. In this work, we present experiments on silicon solar cells where we made annealing treatments of aluminum at two different temperatures (600 and 800°C), and compare the results for cells where there was no aluminum alloying.

2. Experimental

We made silicon solar cells from 300 μm thick Cz silicon wafers with resistivity in the range between 1 and 3 Ω cm. The n+ diffusion was made at 900°C from a $POCl_3$ source in an open tube furnace. After this step, the emitter sheet resistance was between 120 and 140 Ω/square. Silicon nitride grown by plasma enhanced chemical vapor deposition (PECVD) from a mixture of SiH_4 and NH_3 at 250°C was used both as photo-lithographic mask, in order to define the contact fingers at the top, and anti-reflection coating. On the top finger region, a second diffusion was made such that a high phosphorus concentration was obtained under the contacts, reducing in this way the solar cell series resistance. The silicon nitride thickness was around 80 nm, which is appropriate to serve as an antireflection coating on silicon. At the back of the solar cells, aluminum was evaporated and annealed as described. In order to sensitize the silicon surface, immersion in PdCl dried at 120°C was used, and then Ni was deposited by an electroless process to have ohmic contacts at both surfaces. The final structure of the cells is shown in Fig. 1. Such a structure corresponds to what is usually known as a Selective Emitter Solar Cell.

Three groups of solar cells were realized. In the first group (03N), a 1 μm thick aluminum layer was evaporated and annealed in 'forming' gas at 800°C, 40 min. For the second (05N), also 1 μm of aluminum was deposited, but the annealing was made in 'forming' gas at 600°C during 10 min. For the third group (07N) no aluminum was deposited, nor was any annealing made on them. The latter were used only as reference cells.

Dark *I–V* measurements were made as a function of

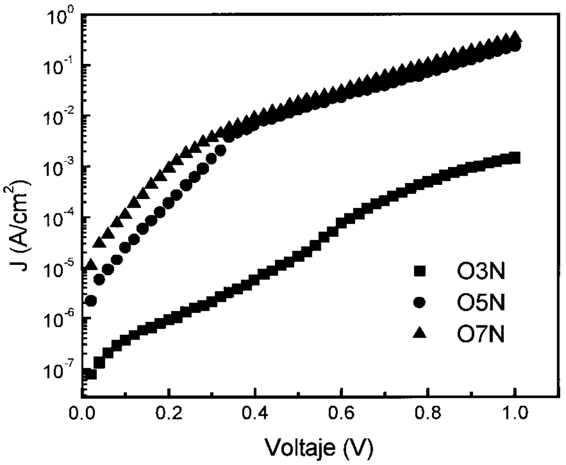

Fig. 2. Typical dark *I–V* curves at 300 K for cells with different aluminum annealing.

temperature, in the range between 77 and 333 K by using a Keithley automatic system. We also measured the *I–V* curves under a tungsten-halogen lamp illumination calibrated to have 100 mW/cm^2 on the cells. This arrangement simulates approximately the AM 1.5 solar spectrum on the cells. We also made quantum efficiency (spectral response) measurements by using a monochromator with a diffraction grating of 1200 lines/mm and calibrated the system with a (1 cm^2) commercial silicon photo-detector. Finally, we also made DLTS measurements using a Bio-Rad 4600DL automatic system.

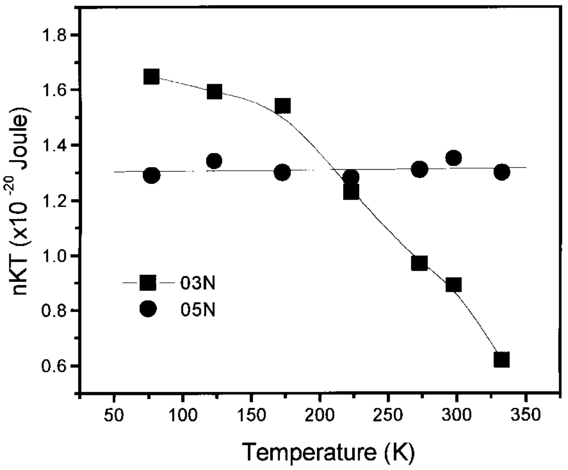

Fig. 3. Product *nkT* as a function of the absolute temperature *T* for cells in the groups 03N and 05N.

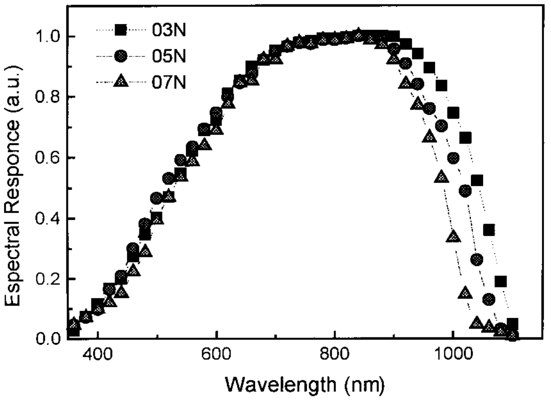

Fig. 4. Relative spectral response measurements for cells in the different groups.

3. Results and discussion

The first important result can be observed in Fig. 2 where the dark *I–V* measurements at 300° K are shown for typical cells of each group. The dark current is significantly smaller for cells of the group 03N as compared to cells of the other two groups. For voltages below 0.4 V, the saturation current seems to be dominated by recombination in the space charge region in all cases, however the ideality factors (n) for groups 05N and 07N were significantly higher than for the 03N group. In order to determine the transport mechanism, we plotted the variation of the product nkT, where n is the ideality factor, k is the Boltzman constant and T is the absolute temperature, as a function of the absolute temperature itself. Typical results for 03N and 05N cells are shown in Fig. 3. Notice that the product nkT is almost constant for cells 05N while for 03N cells there is a variation as a function of absolute temperature. This result means that recombination in the space charge region is enhanced by carrier tunneling for cells 05N, but in the case of cells 03N it seems to proceed through Shockley–Read–Hall deep levels [6,7]. Furthermore, the activation energies for the saturation current densities above 250 K were 0.47 and 0.56 eV, respectively. This result seems to indicate that levels around mid-gap in silicon are very active as recombination centers in this case.

The DLTS measurements gave us further evidence that for cells 05N deep levels might be causing the enhanced recombination in the space charge region. In this case, a trap level 0.34 eV below the conduction band was observed with a concentration around 2×10^{14} cm^{-3}. According to Schroder [7] this level may be associated to iron in silicon and also to thermal stresses during the technological steps. In the case of cells 03N, the resolution of the DLTS system did not allow the determination of the concentration of

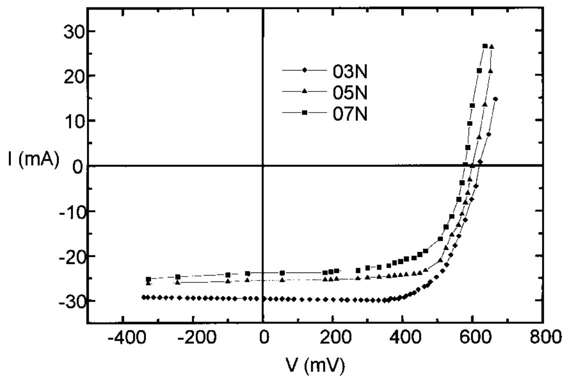

Fig. 5. Typical *I–V* curves for different cells under AM 1.5 simulated light at 300 K.

these levels. In other words, there is a reduction of traps associated to iron, very likely due to the aluminum annealing at higher temperatures. Hence, we should expect improvement not only on the dark current and open-circuit voltage, but also on the minority carrier effective diffusion length, which should cause a better short circuit current for cells annealed at high temperatures.

We confirmed the latter from the typical spectral response measurements shown in Fig. 4, for the different kinds of cells. Notice that cells 03N have a better response for wavelengths above 900 nm, as compared to the other two groups. The effective diffusion length can be estimated from these curves: for cells 07N it was around 86 μm, for cells 05N it was 117 μm and for cells 03N it was around 156 μm, which agreed with our previous expectation. Therefore, cells 03N should not only have better open circuit voltage, but also improved short circuit current with respect to the other two groups, as confirmed by the *I–V* measurements under simulated AM 1.5 illumination shown in Fig. 5. In Table 1 we summarize the results obtained from these curves. Hence, the conversion efficiency improvement, from 10.5% for cells 05N to 12.7% for cells 03N, is achieved because of the annealing of aluminum in forming gas at temperatures around 800°C as compared to conventional processes made at 600°C.

Table 1
Summary of results for the different groups of cells fabricated in this work

Cells	I_{sc} (mA/cm^2)	V_{oc} (mV)	FF (%)	η (%)
03N	29.65	620	69.3	12.7
05N	25.67	600	68.7	10.5
07N	23.70	578	62.0	8.5

4. Conclusions

We have confirmed that annealing aluminum in forming gas at temperatures around 800°C cause the improvement of the electrical characteristics of silicon solar cells. In particular, from DLTS measurements it seems that there is ‘gettering’ of iron impurities introduced during the fabrication processes. The transport of impurities from the bulk to the back surface (alloyed with aluminum) reduces the dark current and increases the effective diffusion length as determined from dark *I–V* and from spectral response measurements, respectively. All these effects cause a global efficiency improvement for cells where aluminum is annealed at 800°C as compared to conventional cells where the annealing is made at 600°C.

These results are encouraging, but we need to improve further our cells by reducing the surface recombination velocity with a good passivating layer. We should have even better spectral response for short wavelengths, allowing us to have better short circuit current densities. We are in the process of optimizing the silicon nitride layer for this purpose [8].

It seems that iron atoms from the bulk move towards the back surface, but annealing for 30 min is not enough to have full metallic ‘gettering’. Dark currents are still dominated by recombination in the space charge region of the cells. Hence, a further study must be made in order to determine the optimum treatment time. This study will be made in the near future, besides observing the effect that the aluminum layer thickness may have upon the efficiency for this kind of silicon solar cells when aluminum is alloyed at such temperatures as reported here. When all these improvements are put together, we expect efficiencies above 16% which is good for an industrial technology such as ours.

Acknowledgements

G. Santana thanks the support provided by the Solid State Electronics Section of the Electrical Engineering Department (CINVESTAV-IPN) during different stays for doing this work as part of his PhD thesis. We also thank Mr Zacarias Rivera-Alvarez for helping us with the DLTS measurements.

References

[1] del Alamo J, Eguren J. Operating limits of Al-alloyed high–low junctions for BSF solar cells. Solid State Electronics 1981;24:415.

[2] Chen CS, Schroder DK. Kinetics of gettering of silicon. J of Appl Phys 1992;12(71):5858.

[3] Narasimha S, Rohatgi A. Optimized aluminum back surface field techniques for silicon solar cells. In: Proceedings of the 26th IEEE Photovoltaic Specialists Conference, Anaheim, CA, 1997. p. 63.

[4] Hartiti B, Muller JC, Slaqui A, Siffert P, Sarti D. Back surface field-induced gettering in multicrystalline silicon. In: Proceedings of the 22th IEEE Photovoltaic Specialists Conference, Las Vegas, NV, 1991. p. 998.

[5] Hieslmair H, McHugo S, Weber ER. Aluminum backside segregation gettering. In: Proceedings of the 25th IEEEE Photovoltaic Specialists Conference, Washington, DC, 1996. p. 441.

[6] Davis JR, Rohatgi A, Hopkins RH, Blais PD, Choudhury PR, McCormick JR, Mollenkopf HC. Impurities in silicon solar cells. IEEE Trans on Electron Devices ED-27 1980;4:677.

[7] Schroder DK. Semiconductor material and device characterization. John Wiley and Sons Inc, 1990.

[8] Santana Guillermo, Morales-Acevedo Arturo. Determination of the optimum silane to ammonia ratio for PECVD SiN:H films used as passivation layers in silicon solar cells. In: Proceedings of the Second World Conference on Photovoltaic Solar Energy Conversion, Vienna, Austria, 1998. p. 2422.

phys. stat. sol. (b) **220**, 209 (2000)

Subject classification: 68.35.Dv; 73.30.+y; 73.40.Ns; S4; S8.13

Barrier Height Behavior for In/CdTe Polycrystalline Junction

M.P. Hernández (a), C.F. Alonso (b), A. Martel (b), E. Casielles (b),
V. Rejón (c), and J.L. Peña[1]) (c)

(a) Instituto de Materiales y Reactivos, Universidad de La Habana,
San Lázaro y L. Vedado, Plaza, Ciudad de La Habana 10400, Cuba

(b) Facultad de Física, Universidad de La Habana,
San Lázaro y L. Vedado, Plaza, Ciudad de La Habana 10400, Cuba

(c) Departamento de Física Aplicada, CINVESTAV-IPN, Unidad Mérida,
A.P. 73-Cordemex 97310, Mérida, Yucatán, México

(Received November 1, 1999)

The chemical composition of CdTe surfaces has been studied for In over polycrystalline CdTe using $I-V$ measurement. The obtained barrier height presents a spatial distribution on CdTe surface and an inhomogeneous barrier height is the cause of the ideal behavior deviation in the $I-V$ curves. Multi-level Fermi pinning within the contact that is produced by aggregate of Te-rich and Cd-rich areas is a consistent explanation for the barrier height inhomogeneities.

Introduction CdTe is a wide bandgap material, known for its wide use in infrared, X-ray and γ-ray detectors. With its large bandgap around 1.40 eV, it is also an important candidate for application in solar energy conversion. For the successful performance of these devices, it is essential to be able to fabricate reproducible, reliable and stable electrical contacts with a high yield material. Therefore, the interest in examining Schottky barrier formation on II–VI semiconductors has increased in recent years [1].

Many papers have reported the barrier height for a wide range of metallic contacts on n-CdTe and p-CdTe [2, 3]. They have shown that barrier height varies within the narrow range of 0.9 to 1.05 ± 0.1 eV. Nevertheless, detailed studies of electrical contacts on n-CdTe have shown that barrier height reaches a value of 0.72 ± 0.02 eV for Te-rich surfaces, and 0.93 ± 0.02 eV for Cd-rich surfaces [4, 5]. Recently moreover, Warslaw and Dharmadasa [6] developed the theory of aggregate area effects of different pinning levels on barrier height, where effective barrier height for a contact can be determined by the area-weighted barrier height of contributory regions. To generalize, if there are N regions, each one of area S_i $(i = 1, 2, ..., N)$ with a barrier height of ϕ_i, contributing to a total contact area S, then the effective barrier height will be given by the equation:

$$S \exp\left(-\frac{e\phi_{\mathrm{eff}}}{KT}\right) = \sum_{i=1}^{N} S_i \exp\left(-\frac{e\phi_i}{KT}\right). \tag{1}$$

---

[1]) Also at CICATA-Altamira, IPN, México.

This is equivalent to N diodes acting in parallel and the effective barrier height is determined by the area-weighted barrier height of contributing regions.

This model permits them to demonstrate that the appearance of different barrier heights for metallic contacts on n-CdTe, prepared in the same way, are provoked by a multi-level Fermi pinning problem within the contact, having the net effect of different diodes acting in parallel [7, 8].

In this paper, the barrier height, the ideality factor and the series resistance from polycrystalline Schottky In/CdTe diodes are obtained from $I-V$ measurements. The acquired barrier height presents a spatial distribution on the CdTe surface. The ideality factor is not equal to unity for all diodes. This result was interpreted as an inhomogeneous barrier height. Multi-level Fermi pinning within the one contact that is produced by an aggregate of Te-rich and Cd-rich areas, is a consistent explanation for the inhomogeneous barrier height. It is using the theory of aggregate area effects of different pinning levels on barrier height [6], that the chemical composition of the CdTe surface is characterised.

Experimental Details The CdTe was grown by double closed-spaced sublimation (DCSS) onto graphite substrates. The DCSS technique consists in two stages of CSVT technique, and has been reported by Martel et al. [9]. The as-grown CdTe has a film thickness of about 10 μm and a resistivity between 10^4 to 10^7 Ωcm. The In metal depositions were performed by the evaporation of a tungsten filament. All samples were thermically treated at 300 °C in a vacuum of 10^{-5} Torr for 1 min. A circular contact array, as shown in Fig. 1a, was constructed on the CdTe, where each diode had an area of 1.223×10^{-6} m^2. The $I-V$ measurements were fully automated by computer control. A Keithley autoranging picoampmeter 485 and a Keithley electrometer/multimeter 619 were used for dc current and voltage measurements, respectively. A Valhalla Scientific Programmable Precision 2701C was used as an external power supply.

Discussion To extract barrier heights from $I-V$ experimental curves, it was assumed that the thermoionic mechanism was dominant. The current is given by

$$I = SA^{**}T^2 \exp\left[-\frac{q(\phi_{\mathrm{B0}} - \Delta\phi)}{kT}\right] \exp\left[\frac{q(V - IR_{\mathrm{s}})}{nkT}\right] \left[1 - \exp\left[\frac{-q(V - IR_{\mathrm{s}})}{kT}\right]\right], \tag{2}$$

where S is the contact area, A^{**} is the modified Richardson constant, R_{s} is the series resistance, $\phi_{\mathrm{eff}} = \phi_{\mathrm{B0}} - \Delta\phi$ is the effective barrier height, $\Delta\phi$ is the image force lowering and n is the ideality factor.

In Fig. 1b, the $I-V$ curves from some of the Schottky diodes can be seen, corresponding to the contact array in Fig. 1a. All of the diodes have a high series resistance. The Lien [10] and Werner [11] methods were applied, allowing the extraction of the ideality factor, series resistance and barrier height for the plotting of auxiliary functions. The results are shown in Table 1. As can be appreciated in Table 1, the results reached by both methods are similar. Nevertheless, a variation of ϕ_{eff}, n and R_{s} is observed between the diodes.

The high values of R_{s} were expected due to the high resistivity of the polycrystalline CdTe grown by DCSS. The ideality factor not being equal to unity, indicates a deviation

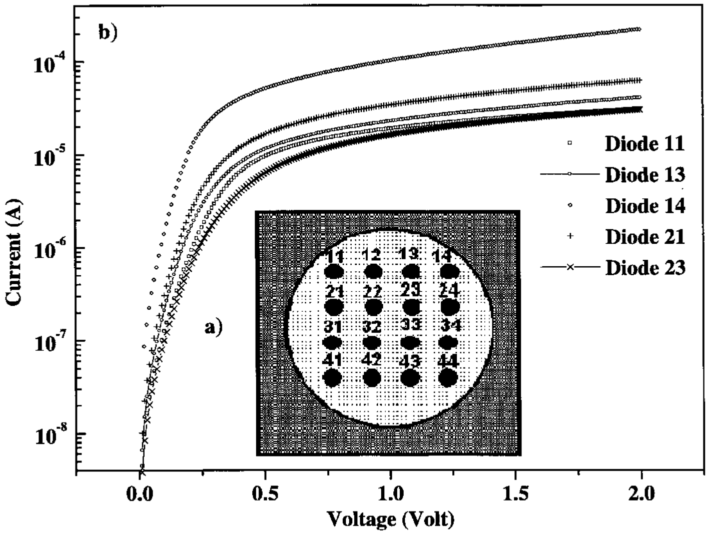

Fig. 1. a) Array of the circular contact of In/CdTe. b) *I–V* measurements obtained in In/CdTe diodes

in the ideal behaviour of the Schottky diode. This behavior is fundamentally caused by the presence of other transport mechanisms (recombination and tunneling), the force image and inhomogeneous barrier height [7, 8, 12]. However, the high resistivity of the CdTe polycrystalline film corresponds to a low carrier concentration. For this reason, conditions do not exist for the presence of tunneling mechanisms. On other hand, a recombination current for low voltage values was rejected, because on being substracted from the *I–V* experimental curve, no appreciable changes could be discerned [13]. Finally, the image force lowering is much less than the involved experimental error ($\approx$0.002 eV).

However, the known Fermi level pinning that appears in CdTe, cannot be justified in the MIGS model, as has been widely argued by Spicer and co-workers [3]. The possibility that the defects have an influence on the Schottky barrier formation on CdTe has been put forward by various authors [14, 15]. The defects of Te_{Cd} antisite and Te vacancy associated with the Te out-diffusion and/or reaction frequency observed at metal/CdTe interfaces can be involved in the Fermi level movement on CdTe [2, 16]. Other

Table 1
The n, R_s and ϕ_{eff} values for some In/CdTe diodes

Werner				Lien		
diodes	n	ϕ_{eff} (eV)	R_s (Ω)	n	ϕ_{eff} (eV)	R_s (Ω)
11	1.93 ± 0.08	0.751 ± 0.001	15995 ± 10	1.86 ± 0.01	0.756 ± 0.010	16998 ± 5
12	2.07 ± 0.09	0.758 ± 0.001	15391 ± 10	2.06 ± 0.01	0.761 ± 0.009	15601 ± 4
13	1.51 ± 0.01	0.739 ± 0.001	19527 ± 30	1.26 ± 0.01	0.741 ± 0.020	21714 ± 6
23	1.97 ± 0.10	0.755 ± 0.030	31859 ± 30	1.94 ± 0.01	0.757 ± 0.030	32170 ± 10
32	2.09 ± 0.01	0.752 ± 0.001	21925 ± 30	2.14 ± 0.02	0.755 ± 0.030	22620 ± 10
33	1.78 ± 0.01	0.755 ± 0.001	34039 ± 90	1.79 ± 0.04	0.756 ± 0.090	33487 ± 30

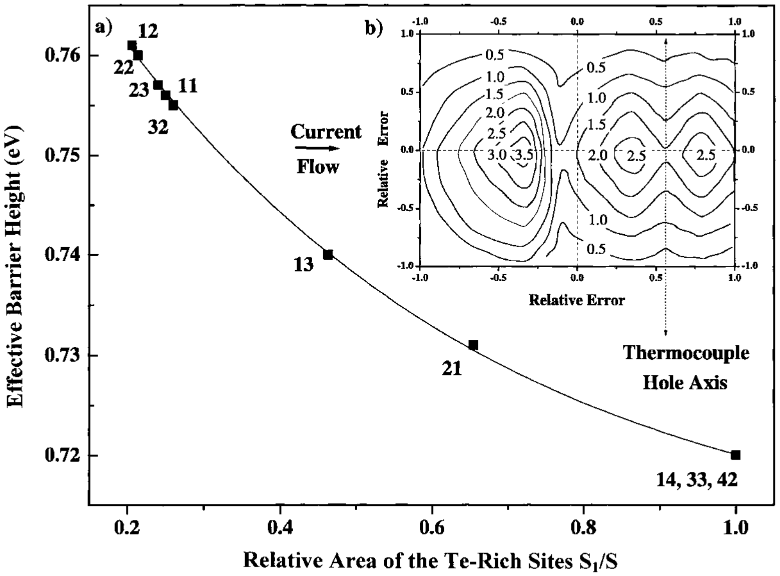

Fig. 2. a) Relative area of Te-rich sites S_1/S. b) Chemical composition of the CdTe surfaces

defects that may have an influence on Fermi level movement that can involve Cd are: $\mathrm{Cd_{Te}}$ antisite and Cd vacancy. These results can be related to enriched regions of Te and Cd, reported by Warslaw and Dharmadasa [6]. For these, a corresponding barrier height of 0.72 and 0.93 eV, respectively, can be found.

Taking into account that the CdTe grown by CSVT and consequently by DCSS, is a material where a high degree of defects, linked to enriched zones of Cd and/or Te, can be observed, we have considered that our contacts can present a mixture of both regimes. In this way, if an area S_1 is enriched by Te and another area S_2 enriched by Cd, then in the total area of contact S ($S = S_1 + S_2$) the effective barrier height will be an intermediate value between 0.72 and 0.93 eV. Or rather, the diodes are acting in parallel in the contact. Applying the theory of aggregate area effects of different pinning levels on barrier height [6], the distribution of the Te and Cd regions is obtained on the surface of CdTe.

Figure 2a shows the relationship between barrier height and the relative area of enriched Te. A notable non-uniformity of the chemical composition of the surface is appreciated. In Fig. 2b, the level curves associated to the variation of barrier height with regard to 0.72 eV can be seen; as can be perceived the composition of Te increases towards the top edge of the sample. This behavior can be related to the temperature distribution across the graphite substrate-heater due to the local-point current entrance (see Fig. 1 of the above cited work [9]).

Conclusions This study indicates that there are problems associated with non-uniform surface effects for metal/CdTe polycrystalline that is grown by DCSS. Hence the reproducibility and the yield of the final product may be seriously affected and therefore the material surface requires extremely careful preparation.

Acknowledgements The authors would like to thank Ing. F. Chale and Ing. O. Gomez for help with automatization of $I-V$ measurements and mechanical support, respectively. We wish also to thank D. Curshen for useful discussions and for proofreading the manuscript.

References

[1] L.M. Woods, D.H. Levi, V. Kaydanov, G.Y. Robinson, and R.K. Ahrenkiel, Proc. 2nd World Conf. and Exibition on Photovoltaic Solar Energy Conversion, Vienna (Austria), July 6 to 10, 1998 (p. 561).
[2] D.J. Friedmann, I. Landau, and W.E. Spicer, Phys. Rev. B **37**, 731 (1988).
[3] A.K. Wahi, K. Miyano, G.P. Carey, T. Chiang, I. Lindau, and W.E. Spicer, J. Vac. Sci. Technol. A **8**, 1926 (1990).
[4] I.M. Dharmadasa, J.M. Thornton, and R.H. Williams, Appl. Phys. Lett. **54**, 137 (1989).
[5] Z. Zobiesierki, I.M. Dharmadasa, and R.H. Williams, Appl. Phys. Lett. **53**, 2623 (1988).
[6] R.S. Warslaw and I.M. Dharmadasa, Internat. J. Electronics **81**, 59 (1996).
[7] I. Ohdomari and K.N. Tu, J. Appl. Phys. **51**, 3735 (1980).
[8] T.R. Tung, Phys. Rev. B **45**, 13509 (1992).
[9] A. Martel, R. Castro-Rodríguez, E. Purón, M. Zapata-Torres, and J.L. Peña, Rev. Mex. Fís., to be published.
[10] C.D. Lien, F.C.T. So, and M.A. Nicolet, IEEE Trans. Electron. Devices **31**, 1502 (1984).
[11] J.H. Werner, Appl. Phys. A **47**, 291 (1988).
[12] E.H. Rhoderick and R.H. Williams, Metal Semiconductor Contacts, 2nd ed., Clarendon Press, Oxford 1988.
[13] M.P. Hernández, C.F. Alonso, and J.L. Peña, phys. stat. sol. (b) **220**, 789 (2000) (this issue).
[14] L.J. Brillson, C.F. Brucker, N.G. Stoffel, A. Katnani, R. Daniels, and G. Magaritondo, Physica **117/118B**, 848 (1983).
[15] I.M. Dharmadasa, W.G. Herrenden-Harker, and R.H. Williams, Appl. Phys. Lett. **48**, 1802 (1986).
[16] M.S. Daw, D.L. Smith, C.L. Swarts, and T.C. McGill, J. Vac. Sci. Technol. **19**, 508 (1981).

phys. stat. sol. (b) **220**, 261 (2000)

Subject classification: 61.10.Nz; 61.16.Ms; 68.55.Jk; 68.55.Nq; S8.11; S8.13; S10.15

Depth Profiling Study of the CdTe/CdS/ITO/Glass Heterostructure with AES and GIXRD

A. MARTEL[1] (a), F. CABALLERO-BRIONES (b), A. I. OLIVA (c),
R. CASTRO-RODRÍGUEZ (b, c), A. IRIBARREN (c), P. BARTOLO-PÉREZ (b, c),
and J. L. PEÑA (b, c)

(a) Facultad de Física, Universidad de la Habana, San Lázaro y L. Vedado, 10400 La Habana, Cuba

(b) CICATA-IPN, Legaria 694, Col. Irrigación, 11500 México D.F., Mexico

(c) Applied Physics Dept., CINVESTAV-IPN, AP 73, Cordemex, 97310 Mérida, Yucatán, México

(Received November 1, 1999)

In this work we use Auger electron spectroscopy depth profiling and grazing incidence X-ray diffraction (GIXRD) to study chemical composition and structure of the CdTe/CdS/ITO/glass heterostructure. The CdS layer was deposited on ITO ($In_2Sn_2O_{7-x}$) substrates by chemical bath deposition and the CdTe film was deposited by double-step close space sublimation. We found by AES profiling a strong intermixing at the CdS/ITO and CdS/CdTe interfaces, confirmed by GIXRD and evidences of two diffusion steps for the CdS into the ITO matrix. Additionally, the CdS/ITO structure was separately investigated in order to know the influence of the substrate roughness on the heterostructure conformation. The morphology of the ITO substrate and the as-deposited CdS layer was studied by atomic force microscopy. The use of GIXRD showed to be useful to study the entire CdTe/CdS/ITO/glass heterostructure. The ITO roughness has proved to be an influencing factor in the structural features and suggested that CdS roughness can also influence the observed composition profiles.

Introduction Recently, important progress has been reached in the elaboration of low-cost solar cells based on CdTe/CdS heterostructures [1, 2]. These advances were accomplished by using different techniques, such as close-spaced sublimation (CSS) [1, 2], electrodeposition [3], physical vapor deposition [4] and screen printing [5]. In all these low-cost techniques, at least a relatively high temperature step is necessary during the cell processing. CdTe/CdS solar cells prepared under similar conditions often have different efficiencies. However, the exact reason for this non-reproducibility is not fully understood. It has been speculated that the surface and interface properties of CdTe/CdS heterostructures may have significant influence on the cell performance [4, 5].

For the analysis of the phases present in the heterostructures, techniques like Auger electron spectroscopy (AES) [6] and secondary ion mass spectroscopy (SIMS) [4, 5] have been generally employed, with the subsequent destruction of the device. Direct phase analysis by X-ray diffraction (XRD) could be used to know the crystalline phases formed in the CdTe/CdS/ITO/glass heterostructure. Grazing incidence X-ray diffraction

---

[1] Corresponding author; e-mail: amartel@ff.oc.uh.cu

(GIXRD) is a technique suited for the study of film layers, because the incidence angle of the X-ray beam can be varied and thus the penetration depth of the X-rays [7, 8]. Applying this principle for a conventional X-ray diffractometer system in which the angle θ is on a fixed position and 2θ is pivoting on a goniometer circle, the contribution to the Bragg reflections are originated from the planes of crystals inside the sample and not parallel to its external surface.

In this work we combine GIXRD and AES depth profiling to characterize CdS/ITO/glass and CdTe/CdS/ITO/glass heterostructures and to assess their structural and chemical properties, especially at the CdS–ITO and CdTe–CdS interfaces. Additionally, the morphology of the ITO substrate and the CdS layer as a function of the ITO roughness is studied by atomic force microscopy (AFM).

Experimental Details The substrates used were Corning 7059 glass coated by ITO ($In_2Sn_2O_{7-x}$) purchased from Valley Research. A thin layer of CdS was deposited on the substrates by chemical bath deposition (CBD), as described elsewhere [9]. The resultant films were pale-yellow and highly adherent. After removal from the CdS deposition bath, the substrates were ultrasonically cleaned in deionized water to remove any loosely adhered particle. The CdS layer was then removed from the back of the substrate with 0.5 N HCl, rinsed, dried, and loaded into the deposition chamber.

To point out the role played by the ITO substrate roughness on the CdS layer properties, we increased the ITO roughness by HCl etching at different times before CdS deposition. On these substrates we deposited a thin CdS layer of about 70 nm by CBD. We measured the roughness of the substrates by AFM and compared it with the CdS one. AES depth profiling was also performed in order to assess the interfacial properties of these structures.

The CdTe layer was prepared by the double-CSS technique described in a previous work [10]. The source plate used was made on ITO/glass substrate using 99.999%-pure CdTe powder kept at 700 °C in a flux of H_2 at a pressure of 20 mbar. The substrate temperature was 600 °C and the growing time 5 min. Before the CdTe growth, both the CdS/ITO/glass substrate and the source were thermally annealed in H_2 flux at 20 mbar during 10 min. The source was kept at 350 °C and the substrate at 400 °C; during this step partial CdS evaporation could take place. The CdTe deposition is achieved in He/O_2 flux at a total pressure of 16 mbar. The CdS/ITO/glass substrate temperature was of 625 °C and the CdTe source temperature was kept at 675 °C. In order to have enough thin CdTe film, the growing time was only 20 s. The complete device was studied by GIXRD at different incidence angles and by AES depth profiling.

The GIXRD measurements were performed in a D5000 Siemens automatic X-ray diffractometer with non-filtered CuK_α radiation source. Special care was taken concerning the stability and repetition of the measurement conditions of one pattern to another. The penetration depth of the X-ray beam at the different incidence angles was calculated using the software included in the D5000 Siemens diffractometer. The AES depth profiles were performed in a Perkin-Elmer PHI 560/ESCA-SAM system with a double cylindrical mirror analyzer and a base pressure of approximately 2×10^{-9} Torr. For the analysis a 3 keV Ar^+ beam at 200 nA current was used. An erosion rate of 10 nm/min was estimated from previous experiences. The AFM images were taken at room temperature, using an AFM Auto-Probe CP in the constant force mode with the same tip-cantilever and the same gain in the feedback

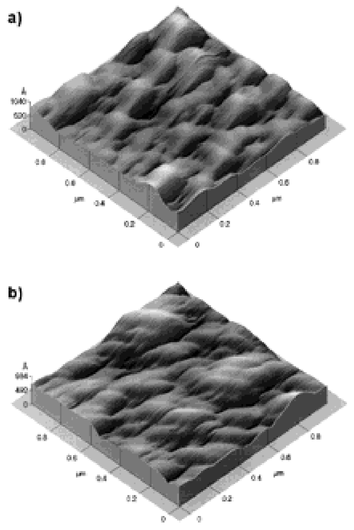

Fig. 1. AFM images of the CdS/ITO structure: a) as-purchased ITO substrate, b) as-grown CdS layer

loop. Three 1×1 μm^2 images of different zones of the sample were taken and analyzed using the Proscan software.

Results and Discussion

ITO-roughness effect on the CdS/ITO structure We studied the surface morphology of the ITO/glass and CdS/ITO/glass structures by AFM. To do this the roughness of the ITO substrate was varied by HCl chemical etching during 30, 60, 90 and 120 s. Figure 1a shows the surface of the as-purchased ITO substrate, while Fig. 1b corresponds to the as-grown CdS/ITO/glass structure. From this figure one can note that the CdS surface roughness is slightly less than the ITO substrate; some holes are filled with CdS, but the surface does not show large changes. The above relation between ITO substrate and CdS/ITO structure was observed for large ITO roughness as shown in Fig. 2 where the rms-roughness of the CdS layer is plotted versus rms-roughness of the ITO substrate. A linear relationship can be noted between the ITO roughness and the CdS one. The slope <1, indicates that the CdS fills the "holes" caused by the attack, tending to diminish or equalize the ITO roughness as we reported in a previous work [9].

Figure 3 shows the AES depth profiles of CdS/ITO/glass prepared with as-purchased (a) and 120 s HCl-etched (b) ITO substrates. In Fig. 3a the Cd and S signals begin to decrease at an estimated thickness of 20 nm. At this time, the O, Sn and In signals begin to rise, indicating that some intermixing took place at the interface. This interface has an estimated width of ≈ 20 nm, but the Cd and S tails seem to be extended deep inside the ITO substrate, in contrast with the Sn, In and O signals that finish at the same moment that Cd and S begin to decrease. This behavior suggests different diffusion speeds for In and S. Figure 2b shows a more extended and intermixed interface

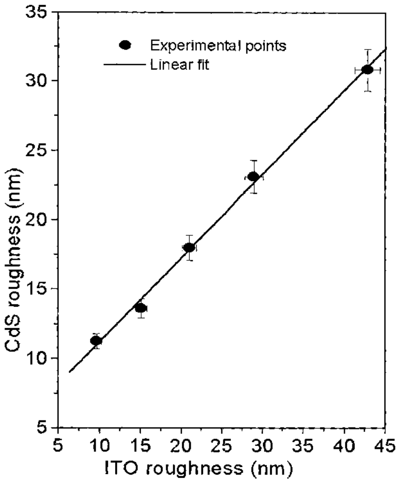

Fig. 2. Relationship between the roughness of the ITO substrate and the CdS layer deposited on it. To achieve different roughness the ITO substrates were etched with HCl between 30 and 120 s

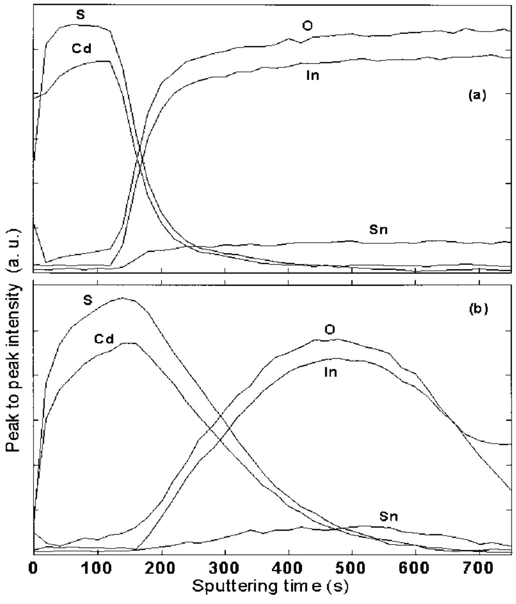

Fig. 3. AES depth profile of the CdS/ITO structure with a) as-purchased ITO, b) 120 s HCl etched ITO substrate

(≈40 nm) with the same behavior in the S and Cd signals, that are still present at about 100 nm. The detailed study of the diffusion process of CdS into ITO substrates will be treated in a future work.

CdTe/CdS/ITO/glass heterostructure

AES depth profiling Figure 4 shows the AES depth profile of the CdTe/CdS/ITO/glass heterostructure. CdTe thickness is about 600 nm, taken from the free surface to the crossing with the sulfur signal, but tellurium is still present at a depth of about 800 nm. At this point, the In, O and Sn signals begin to rise, indicating that there is not a single CdS layer, but a mixture of CdTe–CdS and CdS–ITO alloys, about 300 nm thick each one. Sulfur and cadmium remain present in the ITO matrix at a depth of 1400 nm. This strong CdS–ITO intermixing could take place during the CdS/ITO annealing previous to the CdTe deposition or during the deposition itself, but as we already demonstrated, some degree of intermixing took place in the as-grown structure. By separating the sulfur profile using a two-gaussian fit, it can be seen that the two suggested sulfur diffusion processes take place. The higher and narrower profile corresponds to the CdS diffusion or intermixing during the CdTe deposition, and it is symmetric with respect to the CdS diffused in the CdTe. The wider and smaller profile corresponds to the CdS diffusion in the ITO matrix during the annealing [4, 9, 11].

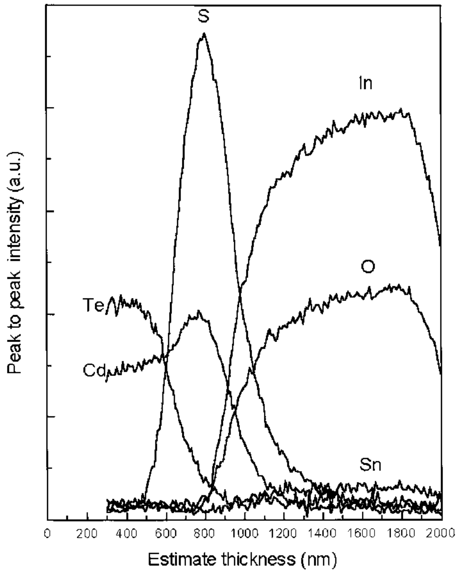

Fig. 4. AES depth profile of the entire CdTe/CdS/ITO/glass heterostructure. Ar^+ beam at 3 keV and 200 nA, with an estimated erosion rate of 10 nm/min was used. During the first 30 min (300 nm) the AES signals were not registered

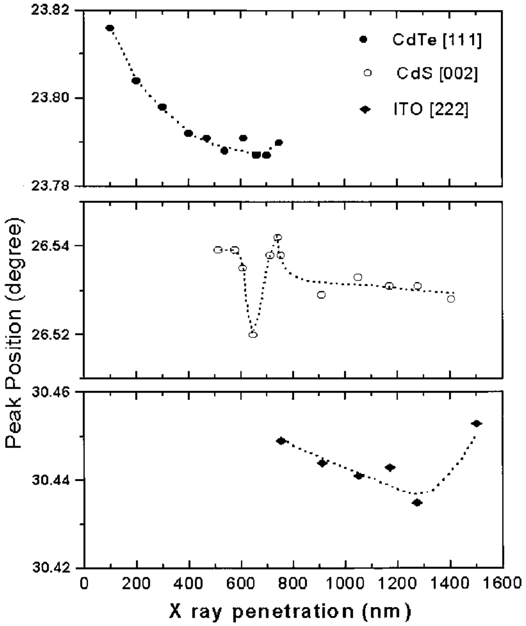

Fig. 5. Peak positions (2θ) of the CdTe(111), wurzite-CdS(002) and ITO(222) peaks obtained from the GIXRD profile. The X-ray penetrations were calculated using the Absorb software included in the Siemens D5000 difractometer and employing $G(x) = 0.90$

On other hand, the formation of a CdTe–CdS mixed interface is a well-known phenomenon, but still not fully understood. The formation of a CdSTe solid solution has been repeatedly proposed [2 to 6, 11, 12], but it has been stated that two crystalline phases might be present at different solubility limits [13]. In our case, the CdTe–CdS interdiffusion might be in fact a physical intermixing of Cd, Te and S during the CdTe deposition: firstly the substrate temperature during this process is high enough (675 °C) to promote the sublimation of the CdS, secondly, the interdiffusion of CdS–ITO takes place. The CdS roughness could also influence the profile information [5], leading to inaccurate determinations of the S-contents of the CdTe–CdS interface. This last consideration also suggests that the major CdS–ITO intermixing observed at higher ITO roughness could be, indeed, due to the same effect. In terms of a solar cell behavior it can be stated that this particular device will not be useful because the CdS window has been practically consumed [1].

Structure of the device by GIXRD The entire device has been studied by GIXRD through the CdTe(111), wurzite-CdS(002) and the ITO(222) diffraction peaks [17]. The diffractograms were taken at the appropriate incidence angles in order to measure the corresponding depths determined by AES profiling. The differences in the estimated penetrations for the AES and GIXRD data can be attributed to the density gradient that exists in the CdTe–CdS and CdS–ITO interfaces (considered in our calculations as the mean between the two materials) and to the differential sputtering rate in the AES system with the different materials considered. Further investigation on these subjects will be treated in future works.

From the diffractograms, the peak positions in the 2θ scale were calculated by fitting the diffraction peaks to gaussian functions and plotted against the X-ray penetration as shown in Fig. 5. The CdTe(111) peak position diminishes with the X-ray penetration reaching a stable value at about 350 nm. The CdS(002) peak at the beginning has a stable position value, then it decreases to a marked minimum at about 650 nm, afterwards it rises to a maximum at about 750 nm and finally reaches a stable value slightly minor than the first one. The above minimum–maximum region just lies in the zone where the sulfur and cadmium signals reach a maximum in the AES profile. The ITO peak does not show noticeable changes in its position value.

The change in the CdTe position from the free surface to its stable value is related with the residual stresses due to the growth [15, 16] and, in the CdS proximity, the decrease in the CdTe position indicates that the CdSTe solid solution could be formed. This confirms the CdTe–CdS interdiffusion shown in the AES profile. For the CdS, the abrupt change in the (002) peak position can be related with the CdS diffusion through the ITO, that may vary its structure, leading to a phase transition zone between cubic and hexagonal CdS at different CdS solubilities [13] as two diffusion processes took place. One can note in the AES profile that this minimum point is coincident with the crossing between the ITO signals and the S signal coming from the CdS diffusion done during the CdTe deposition into the ITO matrix. A more detailed study of the diffraction peaks will eventually require an analysis whether more than one is peak present because it has been reported that CdTe(111) peaks can be convoluted with the CdSTe associated reflections [16]. For the CdS–ITO interdiffusion, a CdInS solid solution could be formed or maybe a small quantity of CdS–ITO stable phases, such as $CdSnO_2$, SnO_2 or SnS_3 mixed with ITO, which have their main diffraction peaks very close to the ITO and CdS ones [17].

Conclusions We have studied the CdTe/CdS/ITO/glass heterostructure by GIXRD and AES profiling. Our results show strong interdiffusion at the CdTe–CdS and CdS–ITO interfaces. There is also evidence of two separate diffusion steps for sulfur in the ITO matrix, due to the heterostructure conformation process itself. We have investigated the role of the ITO roughness in the interfacial properties of the CdS–ITO structure, and shown that the substrate roughness could influence the AES profiling measurements. We have shown that GIXRD is a suitable tool to study this kind of heterostructure.

Acknowledgements The authors would like to thank V. Rejón, M. Herrera, W. Cauich, O. Gómez, E. Corona and R. Sánchez for their technical support and C. Simón and L. Pinelo for their secretarial assistance. This work was partially supported by CICATA-IPN. A. Martel and F. Caballero want to acknowledge the Applied Physics Department at CINVESTAV-IPN Unidad Mérida their research facilities.

References

[1] C. Ferekides and J. Britt, Solar Energy Mater. Solar Cells **35**, 255 (1994)

[2] S. Kamazawa, S. Shibutani, T. Nishio, T. Aramoto, H. Higuchi, T. Arita, A. Hanafusa, K. Omura, M. Murozono, and H. Takakura, Solar Energy Mater. Solar Cells **49**, 205 (1997).

[3] J. Touskova, D. Kindl, and J. Tousek, Thin Solid Films **293**, 272 (1997).

[4] Z. C. Feng, H. C. Chou, A. Rohatgi, G. K. Lim, A. T. S. Wee, and K. L. Tan, J. Appl. Phys. **79**, 2151 (1996).

[5] R. Dhere, D. Albin, D. Rose, S. Asher, K. Jones, M. Al-Hassim, H. Moutinho, and P. Sheldon, Mater. Res. Soc. Symp. Proc. **426**, 361 (1996).

[6] T. Takamoto, T. Agui, H. Kurita, and M. Ohmori, Solar Energy Mater. Solar Cells **49**, 219 (1997).

[7] S. Battaglia, Appl. Surf. Sci. **93**, 349 (1996).

[8] J. S. Rigden, R. J. Newport, and G. Bushnell-Wye, J. Mater. Res. **12**, 264 (1997).

[9] A. I. Oliva, R. Castro-Rodríguez, O. Ceh, P. Bartolo-Pérez, F. Caballero-Briones, and V. Sosa, Appl. Surf. Sci. **42**, 148 (1999).

[10] A. Martel, R. Castro-Rodríguez, J. L. Peña, F. Caballero-Briones, W. Cauich, and E. Puron, Rev. Mex. Fís. **44,** Supl. 3, 254 (1998).
[11] J. Ebothe, J. Appl. Phys. **77**, 233 (1995).
[12] R. Castro-Rodríguez, P. Bartolo-Pérez, D. Pérez-Delgado, F. Caballero-Briones, and J. L. Peña, Mater. Lett. **37**, 281 (1998).
[13] D. W. Lane, G. J. Conibeer, D. A. Wood, K. D. Rogers, P. Capper. S. Romani, and S. Hearne, J. Cryst. Growth. **197**, 743 (1999).
[14] R. Ramírez-Bon, N.C. Sandoval-Inda, F. J. Espinoza-Beltrán, M. Sotelo-Lerma, O. Zelaya-Angel, and C. Falcony, J. Phys.: Condensed Matter **9**, 10051 (1997).
[15] D. Albin, D. Rose, R. Dhere, D. Levi, L. Woods, A. Swartzlander, and P. Sheldon, in: Proc. 26th IEEE Photovoltaic Solar Energy Conf., Anaheim 1997.
[16] H. R. Moutinho, M. M. Al-Jassim, F. A. Abufoltuh, D. H. Levi, P. C. Dippo, R. G. Dhere, and I. L. Kazmerski, in: Proc. 26th IEEE Photovoltaic Solar Energy Conf., Anaheim 1997.
[17] JPCDS, International Center for Diffraction Data, 1997.

Solar Energy Materials & Solar Cells

ELSEVIER Solar Energy Materials & Solar Cells 62 (2000) 369–378

www.elsevier.com/locate/solmat

Gettering effects by aluminum upon the dark and illuminated I–V characteristics of N^+–P–P^+ silicon solar cells

Guillermo Santana[a,1], Arturo Morales-Acevedo[a,*], Andrés Martel[b,2], Luis Hernández[b]

[a] *Departamento de Ingeniería Eléctrica, Centro de Investigación y de Estudios Avanzados del IPN, México, D. F., 07360, Mexico*

[b] *Facultad de Física-IMRE. Universidad de la Habana. 10400, La Habana, Cuba*

Received 1 September 1999

Abstract

Impurity gettering is an essential process step in silicon solar cell technology. A widely used technique to enhance silicon solar cell performance is the deposition of an aluminum layer on the back surface of the cell, followed by a thermal annealing. The aluminum thermal treatment is typically done at temperatures around 600°C for short times (10–30 min). Seeking a new approach of aluminum annealing at the back of silicon solar cells, a systematic study about the effect the above process has on dark and illuminated I–V cell characteristics is reported in this paper. We report results on silicon solar cells where annealing of aluminum was done at two different temperatures (600°C and 800°C), and compare the results for cells with and without aluminum alloying. We have shown that annealing of the aluminum in forming gas at temperatures around 800°C causes improvement of the electrical cell characteristics. We have also made evident that for temperatures below ~ 250 K, the predominant recombination process for our cells is trap-assisted carrier tunneling for both annealing temperatures, but it is less accentuated for cells with annealing of aluminum at 800°C. For temperatures above ~ 250 K, the recombination proceeds through Shockley–Read–Hall trap levels, for cells annealed at both temperatures. Furthermore, it seems from DLTS measurements that there is gettering of iron impurities introduced during the fabrication processes. The transport of impurities from the bulk to the back surface (alloyed with aluminum) reduces the dark current

---

* Corresponding author. Tel.: + 525-747-7000; fax: + 525-754-7697.

E-mail address: amorales@gasparin.cinvestav.mx (A. Morales-Acevedo)

[1] Also at Facultad de Física-IMRE, Universidad de la Habana, 10400, La Habana, Cuba.

[2] Also at Departamento de Física, CINVESTAV. A.P. 14-740, 07000 México, D.F., México.

PII: S0927-0248(99)00158-0

and increases the effective diffusion length as determined from dark *I–V* characteristics and from spectral response measurements, respectively. All these effects cause a global efficiency improvement for cells where aluminum is annealed at 800°C as compared to conventional cells where the annealing was made at 600°C.

Keywords: Aluminum gettering; Silicon solar cells; *I–V* solar cells characteristics

1. Introduction

The increase of unwanted impurity concentration changes silicon solar cell properties in several ways: the substrate can be perturbed by defects, imperfections, clusters, polycrystalline structures and so on. Impurity centers reduce the minority carrier diffusion length due to a rise in recombination centers or by reduction of mobility of the minority carrier as a consequence of scattering. Moreover, unwanted impurities degrade contact–semiconductor interfaces leading to a detriment in the series and shunt resistance values.

It is well known that unwanted impurities like metallic impurities usually produce deep levels in the silicon bulk, deteriorating the minority carrier diffusion length. Hence, metallic impurity gettering is an essential process step for making silicon solar cells. A widely used technique to enhance silicon solar cell performance is the deposition of an aluminum layer on the back surface of the cell, followed by a thermal treatment. It is believed that the improvement is caused by gettering of defects and impurities. Gettering of unwanted impurities from the bulk of the silicon substrate is needed to increase the conversion efficiency of solar cells.

Usually, the p^+ region is formed by aluminum deposition and alloying it at the back of the cell to obtain low contact resistance and to originate an electric field (minority carrier reflector) which reduces minority carrier recombination at the back surface. In order to do this, a solid-phase solution of aluminum in silicon is formed by annealing the deposited aluminum above the eutectic temperature (575°C). Typically, the aluminum is annealed around 600°C for times between 10 and 30 min [1,2]. However, it has been suggested that the great amount of dislocation and stresses induced at this surface, because of this process, could cause a metallic extrinsic gettering effect [3–5] which would be beneficial for the efficiency of solar cells. In order for this gettering phenomenon to occur, the metallic impurities introduced in the material during the fabrication of the cells must diffuse from the bulk to the back melt surface region. There is a high segregation coefficient for these impurities due to the high concentration of defects [1]. In order to help the metallic diffusion and to enhance the segregation, the temperature must be increased to values above the typical aluminum alloying temperature, for example between 700°C and 800°C.

Seeking a new approach to the annealing treatments of aluminum, in this paper we report a systematic study on the effect that a new annealing process, of the aluminum at the back of silicon solar cells, has on dark and illuminated *I–V* characteristics. We report the results on silicon solar cells where annealing of aluminum was done at two different temperatures (600°C and 800°C), and compare the results for cells with and without aluminum alloying.

2. Experimental details

Silicon solar cells were fabricated from 300 μm thick Cz silicon wafers with resistivity in the range between 1 and 3 Ω cm. The n^+ emitter layer was made at 900°C by diffusion from a $POCl_3$ source in an open tube furnace, obtaining emitter sheet resistance between 120 and 140 Ω/square. Using previous developments [6], a silicon nitride layer grown by plasma-enhanced chemical vapor deposition (PECVD) from a mixture of SiH_4 and NH_3 at 250°C was used both as anti-reflection coating and as dielectric mask, to define the contact fingers at the top. On the top finger region, a second diffusion was made such that a high phosphorus concentration was obtained under the contacts, reducing in this way the metal–silicon contact resistivity and thus the solar cell series resistance. At the back of the solar cells, aluminum was evaporated and annealed as described below. In order to sensitize the silicon surface, immersion in PdCl dried at 120°C was used, and then Ni was deposited by an electroless process in order to achieve ohmic contacts at both surfaces. Nevertheless, we did not optimize the contacts obtained in this way. Such a structure corresponds to what is usually known as a Selective Emitter Solar Cell.

Three groups of solar cells (1 cm^2 area) were fabricated. In the first group, baseline cells (C300) with no aluminum layer deposited, nor any thermal annealing was done on them. This group was used only as reference cells. For the second group (C600), 1 μm of aluminum at the back was deposited and the annealing was made in forming gas at 600°C during 10 min. In the third group (C800), also 1 μm thick of aluminum layer was evaporated at the back, but an annealing in forming gas was done at 800°C during 40 min.

Dark I–V measurements were carried out as a function of temperature, in the range between 77 and 333 K, by using a Keithley automatic system. The I–V curves under a tungsten–halogen lamp illumination (calibrated to have 100 mW/cm on the cells simulating, approximately, the AM 1.5 solar spectrum) were also measured. Spectral response measurements were done by using a monochromator with a diffraction grating of 1200 lines/mm, and the system calibrated with a commercial standard silicon photo-diode. Finally, we also made DLTS measurements using a Bio-Rad 4600DL automatic system.

3. Results and discussion

3.1. Dark I–V characteristics

Fig. 1 displays the results of the dark I–V measurements at room temperature for typical cells of each group. One fundamental fact can be observed: the dark current is significantly smaller for cells of the C800 group as compared to cells of the other two

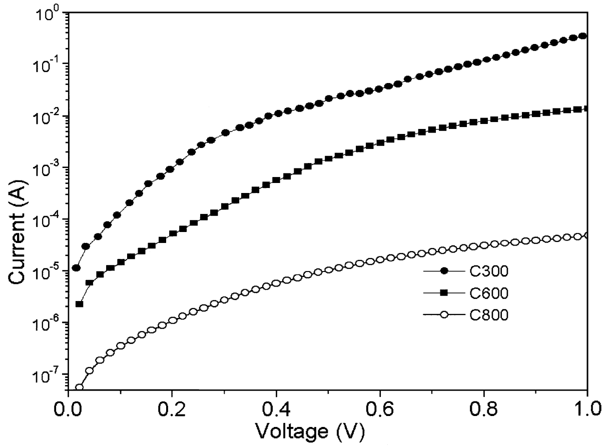

Fig. 1. Typical dark *I–V* curves at room temperature for cells with different aluminum annealing.

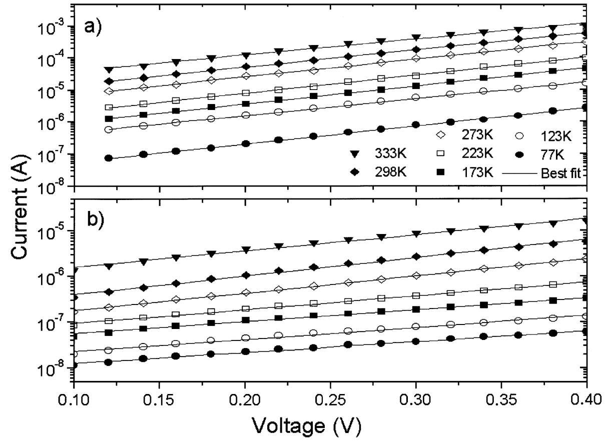

Fig. 2. Dark *I–V* curves for voltages below 400 mV at different temperatures. (a) C600 cells and (b) C800 cells.

groups. Furthermore, for voltages above 0.4 V, in all curves, the series resistance effect determines the behavior of the *I–V* characteristic. For this reason, in the following analysis of the dark *I–V* characteristics we will take into account only voltages up to 0.4 V, which is usually the region where recombination currents are dominant.

In order to recognize the transport mechanism, we measured the cell dark *I–V* characteristics as a function of temperature in the range between 77 and 333 K. Results are shown in Fig. 2(a) and (b) for C600 and C800, respectively. These semi-logarithmic plots seem to confirm that recombination in the space charge region is preferentially enhanced by trap-assisted carrier tunneling, because the dependence between the current and voltage are closely parallel straight lines. However, a careful

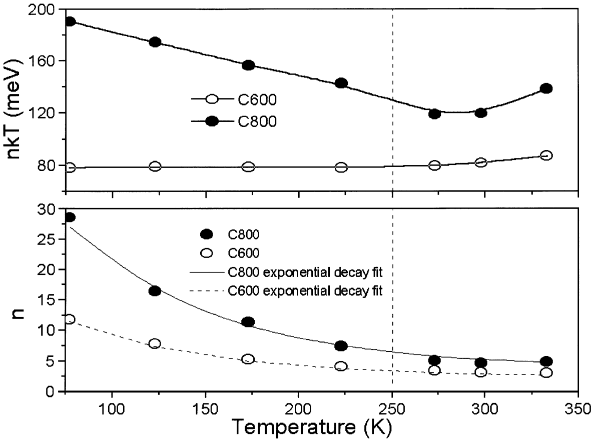

Fig. 3. Product *nkT* and ideality factor *n* as a function of temperature for C600 and C800 cells.

analysis through the dependence of the *nkT* product (where *k* is the Boltzman constant) and ideality factor n as a function of temperature (Fig. 3), drives us to another conclusion. From the above figure, we can see that for temperatures below ~ 250 K, the *nkT* product is constant with temperature for C600 cells. This is the typical behavior of the tunneling mechanism, while the *nkT* product, in the same temperature region, decreases for C800 cells when the temperature increases. For both kinds of cells, the variation of *n* vs. temperature, below ~ 250 K, has an exponential behavior. This fact induces us to assume that the mechanism is identical in both cases, but for the C800 cells, the trap-assisted tunneling is smaller, perhaps due to a lower trap concentration because of a gettering effect by aluminum. For both types of cells, in the temperature range above ~ 250 K, the *nkT* product increases with temperature and the ideality factor has a tendency to reach a constant value. Hence, at these temperatures, recombination seems to proceed through Shockley–Read–Hall deep levels.

In order to verify this assumption, Fig. 4 shows the semi-logarithmic plots of the reverse saturation current (I_r) as a function of $1000/T$. For both types of cells, two different activation energies at the same transition temperature ~ 250 K are found. Furthermore, for $T > 250$ K we also plotted log $(I_r T^{-3/2})$ vs. E_g/nkT (Fig. 5), where E_g is the energy gap at each temperature. The straight lines obtained have slopes close to unity, which corresponds to the Shockley–Read–Hall recombination mechanism [8,9].[3] In this way, we have shown that for $T < \sim 250$ K, the dominant transport mechanism is trap-assisted tunneling of carriers for both kinds of cells, but it is less accentuated for C800 cells due to the gettering effect, which removes trap centers

---

[3] For the Shockley-Read-Hall mechanism, the dark saturation current may be written as: Ir = Const $T^{3/2}$ exp $(-Eg(T)/n(T)kT)$, thus the plot ln (Ir $T^{3/2}$) vs. $Eg(T)/n(T)kT$ has to be a straight line with unitary slope.

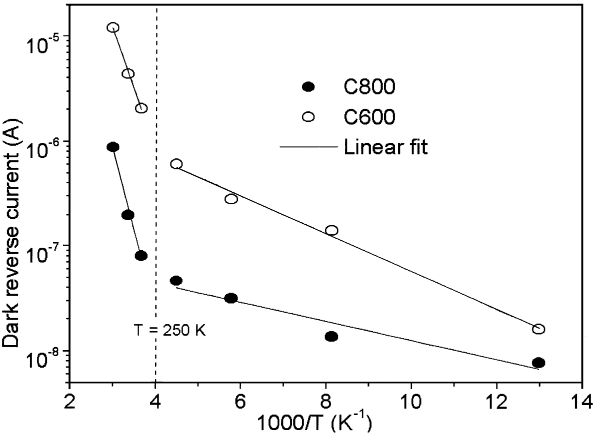

Fig. 4. Arrhenius plot of the dark reverse saturation current as a function of $1000/T$ for C600 and C800 cells.

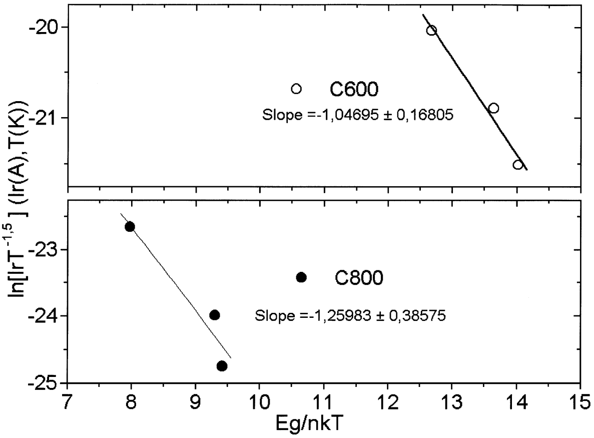

Fig. 5. The log ($Ir\ T - {}^{3/2}$) vs. E_g/nkT plot for $T > 250$ K for C600 and C800 cells.

created by metallic impurities. For $T > \sim 250$ K, however, carrier recombination in the space charge region for both types of cells proceed through Shockley–Read–Hall deep levels.

DLTS measurements gave us further evidence that for the C600 cell, deep levels might be causing the enhanced recombination by trap assisted carrier tunneling in the space charge region. In this case, a trap level 0.34 eV below the conduction band was observed with a concentration around 2×10^{14} cm^{-3}. According to Schroder [9] this level may be associated to iron in silicon and also to thermal stress during the technological steps. In the case of C800 cells, the resolution of the DLTS system did not allow the determination of the concentration of these levels. In other words, there is a reduction of iron associated traps, very likely due to the aluminum annealing at

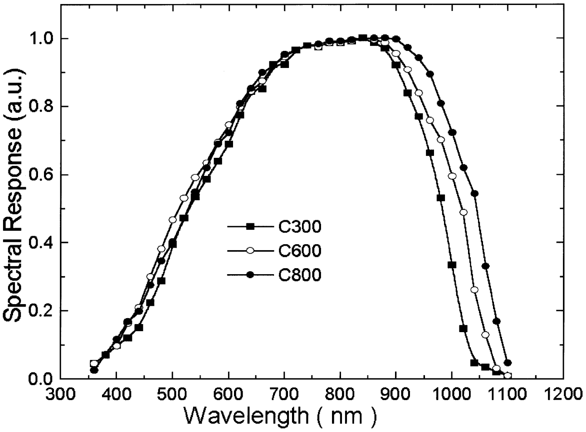

Fig. 6. Spectral response for C300, C600 and C800 cells with different aluminum annealing.

higher temperatures. Hence, we should expect improvement not only on the dark current and open-circuit voltage, but also on the minority carrier effective diffusion length, which should cause a better short-circuit current for cells annealed at high temperatures.

3.2. Illuminated characteristics

Fig. 6 shows the typical spectral response measurements for the different groups of cells. One can note that C800 cell has a better response for wavelengths above 900 nm, as compared to the other two groups. The minority carrier diffusion length was estimated from these curves, giving around 86, 117 and 156 μm for C300, C600 and C800 cells, respectively, which agreed with our previous expectation. Therefore, C800 cells should not only have a better open-circuit voltage, but also an improved short-circuit current regarding the other two groups, as confirmed by the I–V measurements under simulated AM 1.5 illumination as shown in Fig. 7.

The cell parameters were determined from the I–V characteristic equation [7]

$$I = I_{\mathrm{ph}} - I_{\mathrm{r}}\left\{\exp\left[\frac{q(V+IR_{\mathrm{s}})}{n_{\mathrm{r}}kT}\right]-1\right\} - I_{\mathrm{d}}\left\{\exp\left[\frac{q(V+IR_{\mathrm{s}})}{n_{\mathrm{d}}kT}\right]-1\right\} - \frac{V+IR_{\mathrm{s}}}{R_{\mathrm{sh}}}, \tag{1}$$

where I_{ph} is the photocurrent, I_{d} is the reverse dark current related to the quasi-neutral regions of the junction, and I_{r} is the dark reverse recombination current corresponding to carrier recombination through deep levels in the space-charge region of the junction. The other classical parameters, n_{r} and n_{d}, are the diode quality factors for recombination and diffusion currents, respectively, while R_{sh} is the shunt resistance and R_{s} is the lumped effective series resistance.

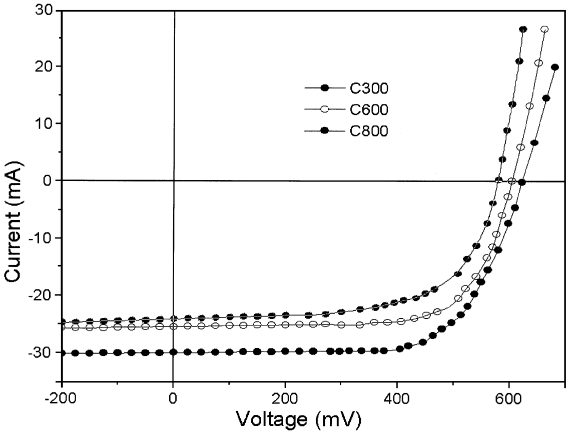

Fig. 7. Typical *I–V* curves under simulated AM 1.5 illumination for C300, C600 and C800 cells with different aluminum annealing.

It was assumed $n_r = 2$ and $n_d = 1$ and then, five iterative equations were necessary to find the cell parameters from Eq. (1). Four of them are the explicit expressions for R_{sh}, R_s, I_{ph} and I_d taken from Eq. (1) and the fifth equation is the zero equation

$$I(I_{root}, V_m) - I_m = 0, \tag{2}$$

where I_{root} is the root and V_m, I_m are the experimental values of the voltage and current at the maximum power point (P_m). As a convergence iteration criterion, the mean square of the difference between the calculated and experimental current values upon the whole *I–V* curves were taken.

Table 1 shows the values of the extracted parameters obtained by this method from the *I–V* illuminated curves. Comparing C600 and C800 cells, an increase of about 4.5 mA cm^{-2} in the short-circuit current (I_{sc}) is observed. However, the highest value of I_{sc} is still low because of the non-optimized antireflection layer. Also, an increase of about 20 mV in open-circuit voltage (V_{oc}) is obtained for C800 cells. Hence, a conversion efficiency (η) improvement, from 10.5% for C600 cells to 12.7% for C800 cells is achieved. Another important fact can be observed in the *I–V* characteristics: the lumped effective series resistance R_s, restrains the fill factor (ff) values for the three groups of cells. In order to appreciate the potentialities of the junction and the bulk of the cells, using an iterative method to solve Eq. (1), the illuminated *I–V* curves are computed for $R_s = 0$ and $R_{sh} = \infty$ (ideal case). A comparison between the real and the ideal extracted parameters is shown in Table 2. We may note that all parameters are improved; especially the maximum power point raises from 10.7 to 12.2 mW for C600 cells and from 12.6 mW to 15 mW for C800 cells, showing the real potential of C800 cells when the contacts should be optimized. From these results, we can confirm that the conversion efficiency enhancement is a consequence of the annealing of aluminum in forming gas at temperatures around 800°C as compared to conventional processes made at 600°C.

Table 1
Cell parameters extracted from the *I–V* illuminated curves

Parameter	Device		
	C300	C600	C800
I_{sc} (mA)	24.3	25.5	30.0
V_{oc} (mV)	590	604	623
P_m (mW)	8.87	10.7	12.6
ff —	0.620	0.699	0.673
η (%)	8.9	10.7	12.6
I_{ph} (mA)	25	25.7	30.1
I_r (A)	9.58×10^{-8}	7.35×10^{-8}	4.60×10^{-8}
I_d (A)	1.98×10^{-12}	1.36×10^{-12}	9.28×10^{-13}
R_s (Ω)	3.590	2.009	2.835
R_{sh} (Ω)	225	633	982
$T = 300$ K	Incident power ≈ 100 mW cm^{-2}		

Table 2
Comparison between real and ideal characteristics for all the cells

Parameter		C300	C600	C800
V_{oc}	Real	590	604	623
(mV)	Ideal	595	607	624
I_{sc}	Real	24.3	25.5	30.0
(mA)	Ideal	25.0	25.7	30.1
P_m	Real	8.9	10.7	12.6
(mW)	Ideal	11,6	12,2	15,0
ff	Real	0.620	0.699	0.673
	Ideal	0.778	0.784	0.799

4. Conclusions

We have shown that annealing aluminum in forming gas at temperatures around 800°C resulted in improved electrical characteristics of silicon solar cells. We have also made evident that for temperatures below ~ 250 K, the dominant carrier recombination mechanism in our cells is by trap-assisted carrier tunneling for both types of cells, but it is less accentuated for C800 cells. For temperatures above ~ 250 K, the carrier recombination mechanism for both kinds of cells, proceed through Shockley–Read–Hall deep levels. Furthermore, from DLTS measurements it seems that because of the aluminum treatment at 800º C there is gettering of iron impurities introduced during the fabrication processes. The transport of impurities from the bulk to the back surface (alloyed with aluminum) reduces the dark current and increases the effective diffusion length as determined from dark *I–V* and from spectral response measurements. Such effects cause a global efficiency improvement in those cells where aluminum is annealed at 800°C, as compared to conventional cells where the annealing is made at 600°C. These results are encouraging, but we need to improve our cells even further by reducing both the series resistance and the surface recombination velocity.

It seems that iron atoms from the bulk move towards the back surface, but annealing for 30 min is not enough to have full metallic gettering. Dark currents at operating cell temperatures are still dominated by carrier recombination in the space charge region of the cells. Hence, further work must be made in order to determine the optimum treatment time. This study will be made in the near future, besides observing the effect that the aluminum layer thickness may have upon the efficiency for this kind of silicon solar cells when aluminum is alloyed at such temperatures as reported here. When all these improvements are put together, we expect efficiencies above 16% which is good for an industrial technology such as ours.

Acknowledgements

G. Santana thanks the support provided by the Solid State Electronics Section of the Electrical Engineering Department (CINVESTAV-IPN) during different stays for doing this work as part of his Ph.D. Thesis. We also thank Mr. Zacarias Rivera-Alvarez for helping us with the DLTS measurements.

References

[1] J. del Alamo, J. Eguren, Solid State Electron. 24 (1981) 415.
[2] C.S. Chen, D.K. Schroder, J. Appl. Phys. 71 (12) (1992) 5858.
[3] S. Narasimha, A. Rohatgi, Optimized aluminum back surface field techniques for silicon solar cells, Proceedings of the 26th IEEE Photovoltaic Specialists Conference, Anaheim, CA, 1997, p. 63.
[4] B. Hartiti, J.C. Muller, A. Slaqui, P. Siffert, D. Sarti, Back surface field-induced gettering in multicrystalline silicon, Proceedings of the 22nd IEEE Photovoltaic Specialists Conference, Las Vegas, NV, 1991, p. 998.
[5] H. Hieslmair, S. McHugo, E.R. Weber, Aluminum backside segregation gettering, Proceedings of the 25th IEEE Photovoltaic Specialists Conference, Washington, DC 1996, p. 441.
[6] G. Santana, A. Morales-Acevedo, Determination of the optimum silane to ammonia ratio for PECVD SiN:H films used as passivation layers in silicon solar cells, Proceedings of the Second World Conference on Photovoltaic Solar Energy Conversion, Vienna, Austria 1998, p. 2422.
[7] J.P. Charles, G. Bordure, A. Khoury, P. Mialhe, J. Phys. D 18 (1985) 2261.
[8] J.R. Davis, A. Rohatgi, R.H. Hopkins, P.D. Blais, P.R. Choudhury, J.R. McCormick, H.C. Mollenkopf, IEEE Trans. Electron Devices ED-27 (4) (1980) 677.
[9] D.K. Schroder, Semiconductor Material and Device Characterization, Wiley, New York, 1990.

Structural characterization of polycrystalline Cd–Te–In films

M. Zapata-Torres
Instituto de Física de São Carlos–USP, Caixa Postal 369, CEP 13560-940, São Carlos, SP, Brazil and CICATA–IPN Unidad Altamira, Km. 14.5 Carretera Tampico-Puerto Industrial Altamira, 86900 Altamira, Tamps., México

R. Castro-Rodríguez[a)]
Departamento de Física Aplicada, CINVESTAV–IPN, Unidad Mérida, A.P. 73, Cordemex, Mérida Yucatan 97310, México

A. Martel
CICATA–IPN Unidad Altamira, Km. 14.5 Carretera Tampico-Puerto Industrial Altamira, 86900 Altamira, Tamps., México and Facultad de Física, Universidad de La Habana, San Lázaro y L. Vedado, A.P. 6426, 10400 La Habana, Cuba

Y. P. Mascarenhas and J. Guevara
Instituto de Física de São Carlos–USP, Caixa Postal 369, CEP 13560-940, São Carlos, SP, Brazil

M. Melendez-Lira
Departamento de Física, CINVESTAV–IPN, Apartado Postal 14-740, México D. F. 07000, México

J. L. Peña
CICATA–IPN Unidad Altamira, Km. 14.5 Carretera Tampico-Puerto Industrial Altamira, 86900 Altamira, Tamps., México and Departamento de Aplicada, CINVESTAV–IPN, Unidad Mérida, A.P. 73, Cordemex, Mérida Yucatan 97310, México

(Received 6 April 2000; accepted 11 September 2000)

Polycrystalline Cd–Te–In films have been grown on glass substrates by close-spaced vapor transport combined with a free evaporation technique and the stoichiometric, structural and electrical properties were investigated as functions of In_2Te_3 concentration added in solid solution into the CdTe structure during In incorporation. Indium was introduced by evaporation during film preparation and the incorporation was controlled by the temperature of the In source. The composition of the films was investigated by Auger electron spectroscopy, showing that, when In concentration increases the Cd concentration decreases they have a similar value (≈22 at.%) at about 750 °C In source temperature. The dark resistivity decreased monotonically four orders of magnitude with the In_2Te_3 concentration and reached a minimum point. From the structural characterization employed it was shown that the In atoms are incorporated in two ways: (I) for as low-In concentration, the In atoms substitute the Cd atoms, decreasing the resistivity; and (II) for high-In concentration, the In atoms form with the CdTe a solid solution like $(CdTe)_{1-x}(In_2Te_3)_x$. The x-ray spectra were calculated for In source temperatures of 550 and 750 °C using structure refinement by the Rietveld method and general structure analysis system software. A good agreement between experimental and calculated spectra was found for both temperatures. [DOI: 10.1116/1.1322643]

I. INTRODUCTION

Semiconductor thin films have specific importance and interest for possible applications to optoelectronic devices such as smart pixel arrays. Therefore, the search for and development of preparation methods which lead to films with sophisticated optical qualities in easily controllable ways have attracted growing interest for both research and technical applications. CdTe is a II–VI semiconductor compound which has been used in several optoelectronic devices such as infrared and gamma radiation detectors, solar cells, etc. The energy of its band gap of 1.5 eV,[1] located at the maximum of the solar energy density incident on the Earth's surface, makes this material very suitable for photovoltaic applications. The incorporation of In atoms at low concentration into doped CdTe monolayers has been achieved by photoassisted molecular beam epitaxy.[2] The effects of heavy doping in CdTe due to high In concentrations has been observed in CdTe polycrystalline films obtained by thermal coevaporation[3] and cosputtering[4] of CdTe and In. In order to explain all the compounds formed by mixing CdTe and In, they are described using the phase diagram of the CdTe–In_2Te_3 system[5] from the In_2Te_3 added in solid solution into the CdTe structure as $(CdTe)_{1-x}(In_2Te_3)_x$ during the incorporation of In. In this system the CdTe has a zinc blende structure (α phase) with lattice parameter $a = 6.481$ Å. As In_2Te_3 is added to the lattice parameter is decreased, and several ternary compounds have been reported: β phase with a chalcopyrite-like structure and $x = 0.42–0.72$ is a very wide phase field to call it CIT (particularly the ternary compound $CdIn_2Te_4$ is formed at x

---

[a)] Electronic mail: romano@mda.cinvestav.mx

$=0.5$), $CdIn_8Te_{13}$ (δ phase) with a cubic structure at $x=0.8$, and $CdIn_{30}Te_{46}$ (γ phase) with a cubic structure at approximately $x=0.94$. This system has been investigated by melting of different concentration of these elements.[5–7]

Close-spaced vapor transport combined with free evaporation (CSVT-FE) is a convenient method by which to grow ternary materials because it is possible to control the temperatures of different compounds separately.[8] It is also cost effective since it can operate at atmospheric pressure under inert gas and uses moderate temperatures; its operation is simple, and films are compact, with few voids. In this work the chemical composition and structural and electrical properties of Cd–Te–In films as a function of In_2Te_3 concentration are presented in order to explain the mechanisms of incorporation of In atoms into the CdTe structure.

II. SAMPLE PREPARATION

All films were prepared in a conventional vacuum evaporation system evacuated by an oil-diffusion pump with a liquid-nitrogen trap, capable of obtaining a background pressure of 10^{-6} Torr. The pressure during evaporation was below 10^{-5} Torr. To obtain Cd–Te–In films we used the deposition technique previously reported by two of the authors[9] consisting of CSVT combined with free evaporation. In our experiments we used high-purity Balzers metallic indium (99.999 at. % pure). The CdTe powder (99.99 at. % pure Balzers) sublimes at a temperature of 500 °C during the growth process, while the In source was varied between 500 and 800 °C, in steps of 25 °C, to achieve different In concentrations. Corning 7059 glass slides were used as substrates. We kept the substrate temperature at 400 °C and the deposition time of 10 min fixed. The control gas used during film growth was Matheson argon 99.999 at. %.

III. MEASUREMENT EQUIPMENT

Compositional measurements were performed by the Auger electron spectroscopy (AES) technique with an ESCA/SAM Perkin Elmer PHI 560 equipped with a double pass cylindrical mirror analyzer, with a base pressure of $\sim 2\times 10^{-9}$ Torr. AES signals were obtained in differential mode using a 3 keV, 0.2 μA electron beam incident at 45° to the surface normal. AES profiles were obtained with an Ar^+ beam with energy of 4 keV and current density of 0.36 $\mu A\,cm^{-2}$, yielding a sputtering rate of about 10 nm/min. The calibration of the sensitivity factor of Auger data was made using stoichiometric CdTe. X-ray diffraction (XRD) measurements in a grazing incidence geometry with 0.5° beam inclination were done under Cu K_α radiation at 40 kV with 35 mA and an aperture diaphragm of 0.2° using a Siemens D5000 x-ray diffractometer with monochromatic radiation ($\lambda=1.5418$ Å). The films were carefully mounted so there was no misalignment. The scanning step of the goniometer was 0.01° with a counting time of 10 s. Scattered radiation passed through an arrangement of horizontal slits to the detector. The dark electrical conductivity of the films was measured at room temperature using the van der Pauw method.

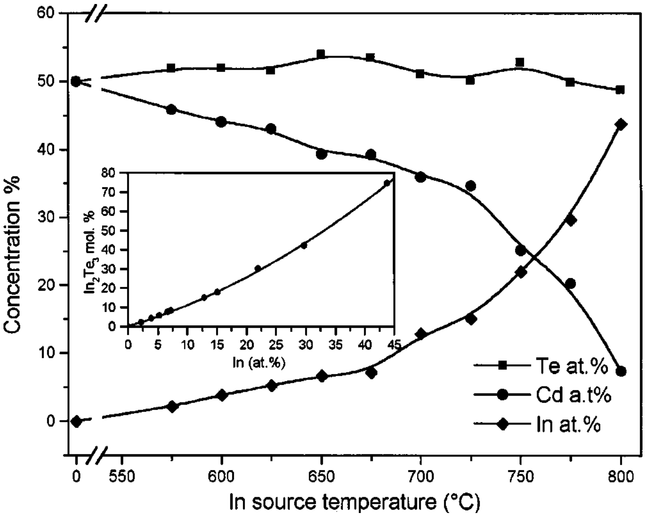

FIG. 1. Atomic composition of the Cd–Te–In films determined by AES vs indium source temperature. The inset shows the relationship between the In at. % and the mol % of In_2Te_3 in CdTe.

Electrical contacts were made with metallic indium previously evaporated onto the film, and are heated 50 °C over the melting point of indium for 5 min under inert atmosphere.

IV. RESULTS AND DISCUSSION

The surfaces of the films were smooth and slightly grayish. All the films firmly adhered to the substrate. The films are polycrystalline, with uniform thickness (around 25 μm). The relative atomic concentration values for all films were determined by AES. Figure 1 shows the relation between atomic concentrations of the films and the In temperature source. From to 550 °C, the In concentration increases monotonically and the Cd concentration decreases while the Te concentration remains constant. Then, the atomic concentration of the In and Cd shows a similar value ($\approx$22 at. %) at about 750 °C. From 700 °C a mixture of the elements Cd, Te and In as a solid solution like $(CdTe)_{1-x}(In_2Te_3)_x$ is formed, as a result of the In_2Te_3 added in solid solution into the CdTe structure. The molar fraction of the In_2Te_3 in the above solution was calculated from the AES data, and the result is shown in the inset. This will be used in the following discussions. On the other hand, the relation between the dark resistivity of the films at 20 °C and the molar fraction of the In_2Te_3 is shown in Fig. 2. The dark resistivity first decreased monotonically four orders of magnitude with the In_2Te_3 molar fraction and reached a minimum point. Afterwards, the resistivity increased to a maximum point, after that it showed a saturation tendency. Similar behavior was found in previous work[10] from a measurement of thermal diffusivity.

To explain the characteristics observed in both Figs. 1 and 2, we analyzed the film structure in detail using x-ray diffraction analysis. Indium can be doped into Cd vacancies of CdTe crystallites substitutionally and can act as a donor during the low-In concentration stage (500–625 °C). The decrease in the film resisitivity at low-In concentration stage is thought to be due to this effect. The resistivity increase over

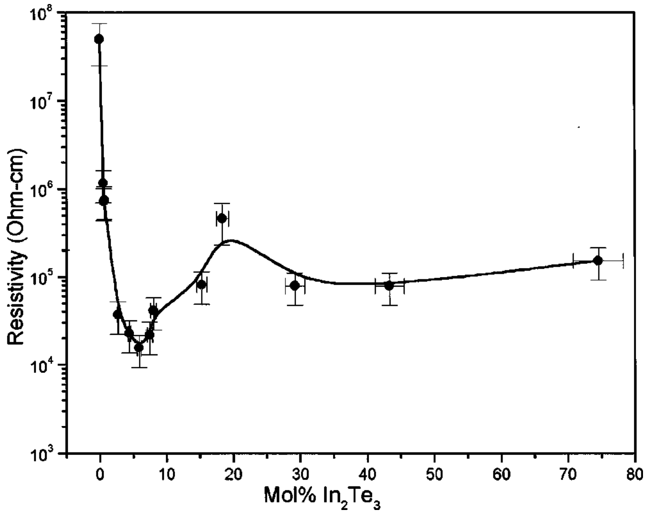

FIG. 2. Dark electrical resistivity of the Cd–Te–In films as a function of In_2Te_3 mol % in CdTe.

the peak may be that the lattice becomes greatly distorted because the radius of the In^{3+} ion (0.92 Å) is smaller than the Cd^{2+} ion radius (1.03 Å), and the distorted lattice may enhance the electron scattering and decrease the mobility. Therefore, a CdTe lattice doped with substitutional In atoms may shrink and become distorted. This can clearly be seen in Fig. 3. Figure 3 displays the normalized three-dimensional (3D) x-ray diffraction pattern showing the evolution of the present structural phases in our samples, from 0 to about 10 mol % In_2Te_3. The films present α phase and the only observed effect is a decrease of the lattice parameter. For In_2Te concentration greater than 10 mol % progressive shifting and deformation of the [111] CdTe peak can be observed and the presence of another peak, which tends towards the position of the $CdIn_2Te_4$ [112] peak. At about 30 mol % of In_2Te_3 both of the peaks are well defined.

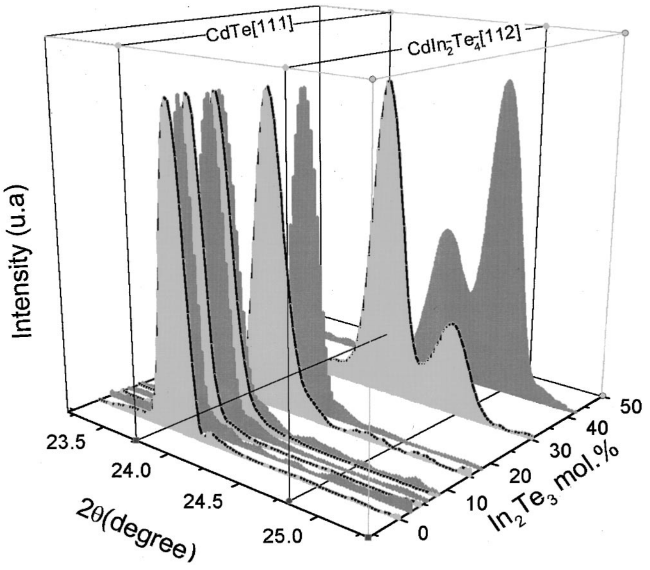

FIG. 3. Three-dimensional normalized x-ray diffraction patterns plotted as a function of the In_2Te_3 mol % in CdTe.

Such behavior is related to the presence of the β phase from 10 to 15 mol % of In_2Te_3. The above results agree very well with the phase diagram for the CdTe–In_2Te_3 system reported by Thomassen *et al.*[5] According to this diagram, for concentrations below 10 mol %, only the α phase can be present. In Cd deficient polycrystalline films like CdTe films, the In can occupy the Cd vacancies in this mol % region. From 10 to 42 mol % In_2Te_3 the α and β phases have to be present. Thus in this region the films are a solid solution of the above phases. Besides the above, we did not find the CdTe [111] peak in the x-ray diffraction pattern of the film grown at In source temperature of 800 °C. It is due to the mol % In_2Te_3 of this film (75 mol %) which lies in the region of the phase diagram where the α phase cannot be present.

Mixtures of a II–VI compound like CdTe and III–VI compound like In_2Te_3 form extended regions of solid solutions. As both components crystallize in the zinc blende lattice, one would expect that the solid solutions are also of zinc blende type. However, because of the stoichiometric ratio of 2:3 for In:Te, one third of the sites in the cation sublattice of In_2Te_3 are vacant. The concentration of these structural vacancies in the solid solutions decreases with an increasing amount of the II–VI component. In the solid solution the content of vacancies will be randomly distributed. The structural vacancies in the cation sublattice, which are caused by the different valences of Cd^{2+} and In^{3+} ions, are characteristic for all solid solutions of II–VI and III–VI compounds.

In fact, the ternary compound $(\mathrm{CdTe})_{1-x}(\mathrm{In_2Te_3})_x$ could be written as $\mathrm{Cd}_{1-x}\mathrm{In}_{(2/3)x}\mathrm{Te}$, and the relation between the lattice parameter and the molar function of In_2Te_3 in CdTe has been reported by Weitze and Leute[7] as

$$a(x)(\text{Å})=6.484-0.336x \quad (0<x<0.7), \tag{1}$$

$$a^*(x)(\text{Å})=6.120+0.455x-0.413x^2 \quad (0.7<x<1), \tag{2}$$

where a is a cubic lattice constant, a^* is a pseudocubic lattice constant, x is a molar fraction of In_2Te_3 in CdTe and from these results we calculated the lattice parameter as a function of the cation vacancies in the solid solutions. Using $\mathrm{Cd}_{1-x}\mathrm{In}_{(2/3)x}\mathrm{Te}$, we can write the cation vacancies (CV) as $\mathrm{CV}=1-(1-x)-(2/3)x=(1/3)x$ where 1 represents the total cation sites, $(1-x)$ are the sites occupied by Cd and $(2/3)x$ are the sites occupied by In. The lattice parameter as a function of CV can be written, with substitution in Eqs. (1) and (2), as

$$a(\mathrm{CV})(\text{Å})=6.484-1.008\ \mathrm{CV} \quad (0<\mathrm{CV}<0.233), \tag{3}$$

$$a^*(\mathrm{CV})(\text{Å})=6.120+1.365\ \mathrm{CV}-3.717(\mathrm{CV})^2$$
$$(0.2337<\mathrm{CV}<0.333). \tag{4}$$

A plot of these theoretical results and the experimental film data are shown in Fig. 4. The theoretical curve and the experiment, in general, agree well. However, we considered it necessary to make a distinction in the region corresponding to the 10 mol % In_2Te_3 value, below which only the α phase is present. This is shown in the inset of Fig. 4. One can see a

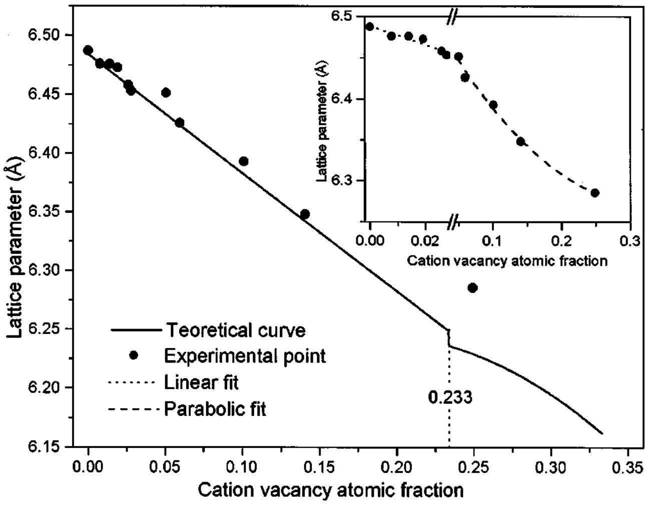

FIG. 4. Lattice parameter as a function of cation vacancy in the solid solution $(CdTe)_{1-x}(In_2Te_3)_x$.

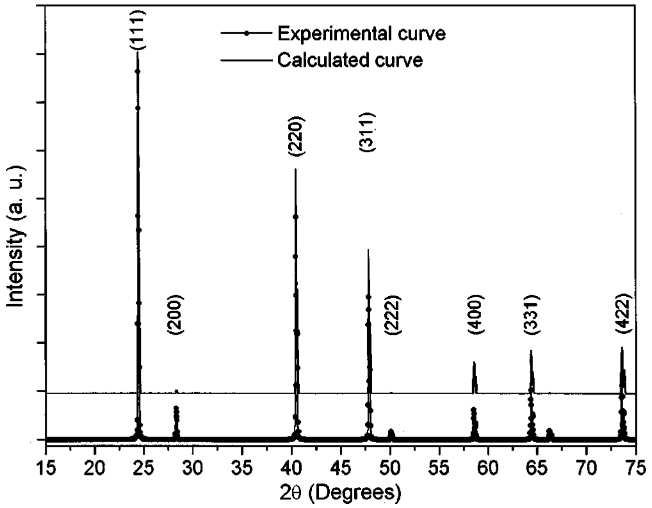

FIG. 5. Rietveld method refined profile of x-ray diffraction data for a sample with an indium source temperature of 550 °C.

linear region corresponding to occupation of the Cd vacancies by In and a parabolic region corresponding to the solid solution. The fitting of the regions is

$$a(\mathrm{CV})(\text{Å})=6.48797-1.10919\ \mathrm{CV}\quad(0<\mathrm{CV}<0.028), \tag{5}$$

$$a(\mathrm{CV})(\text{Å})=6.51452-1.48079\ \mathrm{CV}+2.24766\ \mathrm{CV}^2\quad(0.028<\mathrm{CV}<0.25). \tag{6}$$

The break region of the plot corresponds to the 10 mol % of In_2Te_3.

To explain the results observed in Fig. 4, we had supposed from our x-ray results that the In incorporation into CdTe was made in two ways: (I) for low-In concentration, where the In atoms substitute the vacancies of Cd atoms, and (II) for high-In concentration, where the In atoms form with the CdTe as a solid solution $(CdTe)_{1-x}(In_2Te_3)_x$.

In order to confirm our observation, two representative samples, one for each incorporation mechanism [(I) and (II)], were selected to perform structure refinement by the Rietveld method using the general structure analysis system (GSAS) program.[11] The structures were refined with the space group F-43M. The refined instrumental and structural parameters were peak shape (using a pseudo-Voigt peak profile function), scale factor, background, unit cell parameters, position parameters, isotropic thermal parameters and preferred orientation. We introduced the effect of cation vacancies into the site occupancy factors of the atoms and fixed them. The final refinement cycles yielded conventional reliability factors of $R_{\mathrm{Bragg}}=9.8\%$ and 9.0%, which give irrefutable evidence of our structural model.

The plot of observed and calculated x-ray diffraction patterns is shown in Fig. 5 for the sample with indium source temperature of 550 °C. The curves are vertically shifted. This plot corresponds to the sample of mechanism (I). In this case we supposed that the In atoms substitute for the Cd atoms. We can see the peaks related to the (111), (220), (331), (400), (331), and (422) planes.

Figure 6 shows x-ray diffraction for the sample with In source temperature of 750 °C. We can see the plot corresponding to mechanism II. The curves are vertically shifted. In this refinement we supposed that two In atoms substituted for three Cd atoms, yielding one vacancy. By calculating the lattice constant, we obtained the amount of vacancies present in the solid solution (using Fig. 4). We can see additional peaks related to the (200), (222), and (420) planes. This could be due to the fact that an increase of vacancies increases the relative intensities of these peaks, and to a preferential orientation effect.

In addition to the above models, another model may be considered: many In atoms may deposit at grain boundaries or upon the surface of the film after growth; however, if this

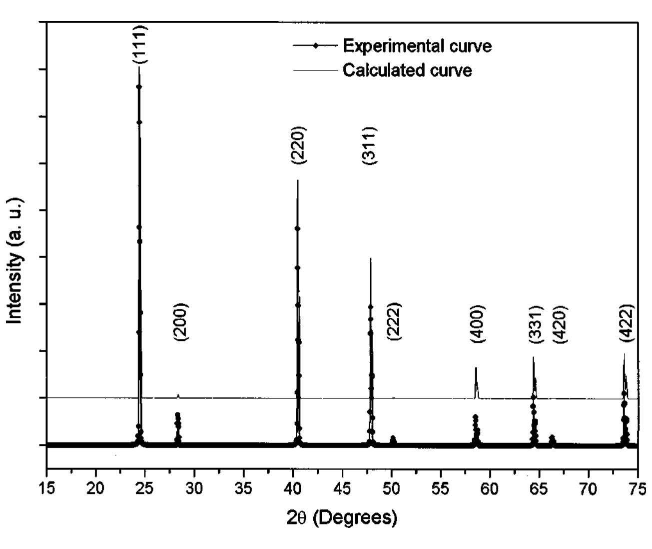

FIG. 6. Rietveld method refined profile of x-ray diffraction data for a sample with an indium source temperature of 750 °C.

is true, the larger peaks corresponding to In should appear in the x-ray-diffraction pattern shown in Fig. 3, and these peaks were not detected in our films as can be seen in Fig. 3.

V. CONCLUSIONS

In summary, all the results obtained from the structural characterization employed indicated that the In atoms are incorporated in two ways: (I) for as low-In concentration, the In atoms substitute for Cd atoms, decreasing the resistivity by four orders of magnitude; and (II) for high-In concentration, where the In atoms form with the CdTe a solid solution like $(\mathrm{CdTe})_{1-x}(\mathrm{In}_2\mathrm{Te}_3)_x$. All the results agree well with the phase diagram for the $\mathrm{CdTe}-\mathrm{In}_2\mathrm{Te}_3$ system.

ACKNOWLEDGMENTS

The authors would like to thank Oswaldo Gómez, Mario Herrera, Victor Rejón, Wilian Cauich, Jose A. L. da Rocha, Jose G. Catarino, and Roberto Sánchez for technical assistance and CONACyT (Mexico) for financial support under Project Nos. 2367PE9509, 5372E, and F586-E9403. One of the authors (M.Z.-T. acknowledges financial support of CONACyT (Mexico) for postdoctoral training at the IFSC-USP Institute and a second author (A.M. acknowledges COFAA-IPN for financial support.

[1] D. de Novel, Philips Res. Rep. **14**, 361 (1959).
[2] R. N. Bicknell, N. C. Giles, and J. F. Schetzina, Appl. Phys. Lett. **49**, 1095 (1986).
[3] T. Hayashi, T. Suzuki, and Y. Ema, J. Appl. Phys. **27**, 1626 (1988).
[4] R. Ramírez-Bom, R. Nuñes-Lópes, F. J. Espinoza-Beltrán, O. Zelaya-Angel, and J. González-Hernández, J. Phys. Chem. Solids **58**, 807 (1997).
[5] L. Thomassen, D. R. Mason, G. D. Rose, J. C. Sarace, and G. A. Schmitt, J. Electrochem. Soc. **110**, 1127 (1963).
[6] D. F. O'Kane and D. R. Mason, J. Electrochem. Soc. **110**, 1132 (1963).
[7] D. Weitze and V. Leute, J. Alloys Compd. **236**, 229 (1996).
[8] M. Zapata-Torres, R. Castro-Rodríguez, A. Zapata-Navarro, J. Mustre de León, and F. J. Espinosa y J. L. Peña, Rev. Mex. Fis. **43**, 429 (1997).
[9] R. Castro-Roríguez, M. Zapata-Torres, A. Zapata-Navarro, A. I. Oliva, and J. L. Peña, J. Appl. Phys. **79**, 184 (1996).
[10] A. Martel, R. Castro-Rodríguez, E. Puron, M. Zapata-Torres, and J. L. Peña, Rev. Mex. Fis. **46**(2), 195 (2000).
[11] A. C. Larson and R. B. von Dreele, Generalized Structure Analysis System, Document No. LAUR 86-748, Los Alamos National Laboratory, Los Alamos (1993).